Synthesis of Acetylenic Carbon Molecules via Pulsed Laser Ablation in Ethanol

by

Nancy Matsu Fujikado

A Dissertation Presented in Partial Fulfillment
of the Requirements for the Degree
Master of Science

Approved April 2018 by the
Graduate Supervisory Committee:

Scott G. Sayres, Co–Chair
Kaushal Rege, Co–Chair
Matthew D. Green

Arizona State University

May 2018

ABSTRACT

New forms of carbon are being discovered at a rapid rate and prove to be on the frontier of cutting edge technology. Carbon possesses three energetically competitive forms of orbital hybridization, leading to exceptional blends of properties unseen in other materials. Fascinating properties found among carbon allotropes, such as, fullerenes, carbon nanotubes, and graphene have led to new and exciting advancement, with recent applications in defense, energy storage, construction, and electronics. Various combinations of extreme strength, high electrical and thermal conductivity, flexibility, and light weight have led to new durable and flexible display screens, optoelectronics, quantum computing, and strength enhancer coating. The quest for new carbon allotropes and future application persists.

Despite the advances in carbon-based technology, researchers have been limited to sp^3 and sp^2 hybridizations. While sp^3 and sp^2 hybridizations of carbon are well established and understood, the simplest sp^1 hybridized carbon allotrope, carbyne, has been impossible to synthesize and remains elusive. This dissertation presents recent results in characterizing a new sp^1 carbon material produced from using pulsed laser ablation in liquid (PLAL) to ablate a gold surface that is immersed in a carbon rich liquid. The PLAL technique provides access to extremely non-thermal environmental conditions where unexplored chemical reactions occur and can be explored to access the production of new materials. A combination of experimental and theoretical results suggests gold clusters can act as stabilizing agents as they react and adsorb onto the surface of one dimensional carbon chains to form a new class of materials termed “pseudocarbynes”. Data from several characterization techniques, including Raman spectroscopy, UV/VIS spectroscopy,

and transmission electron microscopy (TEM), provide evidence for the existence of pseudocarbyne. This completely new material may possess outstanding properties, a trend seen among carbon allotropes, that can further scientific advancements.

ACKNOWLEDGMENTS

I would like to start by expressing my deepest gratitude to my outstanding thesis advisor, Dr. Scott G. Sayres. He is an inspirational mentor and his guidance over the past 3 years has truly proven invaluable. Dr. Sayres is a strong role model, an innovative problem-solver, and an extremely dedicated researcher, who strives to help each one of his students succeed. His dedication and enthusiasm facilitates more than knowledge and skills in his students; it provides us with deep appreciation for excellence and a strong desire to persevere. Dr. Sayres has been my biggest support system and I am truly blessed to have had the opportunity to learn from such a knowledgeable professor. My unforgettable experience as part of the team is largely due to the amazing and caring people that make up the group. I would like to specifically thank Ryland Wala for his assistance throughout the duration of my research. I am proud to have been part of the Sayre's lab and am grateful for all the opportunities and friendships that followed.

I would like to express profound appreciation to my committee members Dr. Kaushal Rege and Dr. Matthew D. Green for their patience and commitment throughout the completion of my thesis. A special thanks goes to Dr. Peter Buseck, I had the wonderful opportunity to learn from his vast expertise and pursue research in a field I wouldn't have otherwise been exposed to. My sincere thanks to Dr. Tim Steimle for his unwavering support and advice, his kind efforts provided me the motivation needed during difficult times. I would like to express my heartfelt thanks to Dr. Armando A. Rodriguez and Dr. Mary Anderson-Rowland for encouraging me to pursue a Masters and seeing my underlying potential.

Finally, I would like to thank my parents for all their support and patience. They have always done the most in providing me with the tools and guidance necessary to overcome any hardship.

TABLE OF CONTENTS

Page

LIST OF TABLES

Table Page

LIST OF FIGURES

Figure Page

Figure Page

Figure Page

Figure Page

Figure Page

Chapter 1

INTRODUCTION

The basis of organic chemistry has always concentrated on carbon molecules and the compounds they form. Elemental carbon is very versatile and has the capability of forming either simple bonds to make molecules like methane, or more complex bonds to form carbon chains. Not only is carbon the most important element for the existence of living creatures, but it has also become increasingly important for nanotechnology and the world of science. Carbon has the unique ability to form an unlimited number of molecular compounds coupled with astonishing properties. Every new discovery made in the carbon field is another step towards extraordinary results. Heightened interest in carbon compounds lies in developing more nanostructured carbon, which exhibit distinct quantum properties that are not otherwise seen in large-scale compounds. This thesis discusses the synthetic method used for acetylenic carbon generation and the importance of gold nanoparticle inclusion. The purpose of this chapter is to introduce carbon nanomaterials and the impact their unique properties have on modern technology.

1.1 NANOSCIENCE

Nanotechnology has taken a strong lead in modern day science and has greatly influenced a vast range of fields, with application seen in medical settings, communications, biotechnology, and energy production.[1] Nanotechnology focuses on the manipulation and formation of objects that restrict at least one dimension to the nanometer scale. Popularity for nanoscience grew throughout the 1970's and 1980's when Dr. Norio Taniguchi coined the term "nanotechnology" while describing the

possibility of precision machining within the atomic scale.[2] Dr. Taniguchi's idea paved the way towards new forms of nanofabrication, particularly, bottom-up and top-down methods. Bottom-up nano-fabrication involves stacking individual atoms onto a substrate, assembling a crystal plane, and giving rise to a nanostructure. This technique is typically carried out in the form of chemical synthesis, developing conditions for self-assembly due to physical forces.[3] On the other hand, the top-down approach begins with a larger macroscopic structure that is etched away until at least one dimension is reduced to a nanometer length scale. In this sense, the building blocks are removed from a substrate to form nanostructures.

The large-scale production of semiconductors, owes much of its success to nanotechnology. For years, the semiconductor industry has incorporated a top-down approach to create nanoscale patterns on wafers, allowing for tunable electrical and optical properties. The strive for smaller technology in the industry is driven by Moore's Law, which states that the number of transistors in a dense integrated circuit doubles every two years. This observation was made by Gordon Moore in 1975 and has proved accurate for several decades, helping semiconductor industries establish long-term plans.[4]

Gold Nanoparticles

Nanoparticles have also gained momentum in recent years as a result of the peculiar qualities attributed to their size. When objects reach the scale of a few nanometers, they begin to exhibit unique properties due to surface and quantum effects.[6,7] Colloidal gold has been a topic of interest for scientists over the past 400 years. The fascinating optical properties of colloidal gold can be traced as far back as

the 4th century A.D. During this period of time, the Roman Lycurgus Cup was discovered, which exhibits a dichroic effect that causes the glass to appear different colors depending on the angle in which light hits the cup and the angle in which it is observed.[8] These strange optical properties are a result of nanosized gold particles embedded within the glass. In 1852, Michael Faraday conducted one of the first scientific studies aimed towards understanding the properties of colloidal gold. His presentation at the Royal Institute in London was titled "Experimental Relation of Gold to Light", and correlated the change in color of colloidal gold from ruby red to purple as a mere variation in particle size.[6,9] Faraday's studies later inspired Gustav Mie's theoretical work to understand the color associated with gold nanoparticles in the 1900's. Mie was the first to calculate the absorption spectrum of gold nanoparticles using classical electromagnetic theory.[10]

Currently, colloidal gold properties are largely investigated for drug delivery purposes in the medical field. However, while bulk gold itself is an inert metal, nanosized gold is known to be one of the most catalytic materials. This characteristic of nanosized gold has lead to complications in the medical field, but greatly increases its value and demand in supplementary applications.[7,11] Gold nanoparticle properties are easily tunable by varying size, shape, or capping them.[12] The ease in tunability is a huge advantage and allows gold nanoparticles to be utilized for bioimaging, sensing, and photothermal therapy, among many other purposes. The functionality of gold nanoparticles is constantly expanding and is developing in diverse areas for use in electronics and optical devices.[11] By embedding nanoparticles into other materials or attaching them to molecules, new and distinct effects are reached that are otherwise unachievable with corresponding bulk materials.[11]

1.2 CARBON ALLOTROPES

Materials singularly composed of carbon atoms, such as diamond or graphite, with no additional atoms terminating or incorporated in the carbon network are called carbon allotropes.[13] Carbon allotropes are different geometric forms of pure carbon that are joined together by strong covalent bonds. The different geometric arrangements and hybridizations provide each allotrope with its own set of unique properties.[14]

Carbon possesses three different types of energetically competitive orbital hybridizations: sp^1, sp^2, and sp^3. Perhaps the most common and well-known allotropes of carbon are diamond and graphite, which are composed of sp^3 and sp^2 hybridizations, respectively. A simple comparison between diamond and graphite highlights the significant impact crystal structure has on their properties. Diamond is known to be the hardest material to naturally form and is exploited in industrial settings for polishing, cutting, and drilling other hard materials.[15] On the other hand, graphite, being extremely soft and slippery, is used in refractory applications as a lubricant. While very different, both materials are entirely composed of pure carbon atoms, however, the difference in crystal structure results in distinct properties.

Currently, all existing carbon allotropes are either sp^2 or sp^3 hybridized molecules. Figure 1.1 illustrates the different carbon hybridizations and the corresponding allotropes. The same sp^3 hybridization that makes up diamond can vary in crystal structure and form differing allotropes, such as, C_8 and Lonsdaleite.[16] However, much of present day research is centered around sp^2 carbon allotropes.

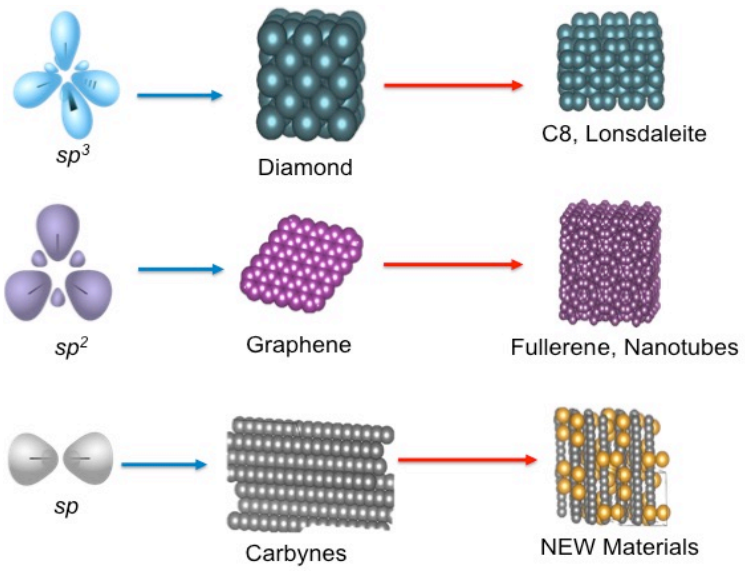

Figure 1.1: Flow chart of sp^3, sp^2, and sp^1 carbon hybridizations showing corresponding carbon allotropes. Modified from [17]

In 1985, during the rise of nanotechnology, Harold Kroto, Richard Smalley and Robert Curl, discovered and isolated a new material found to be entirely composed of carbon.[18] This new material drew massive attention for its size, being only 1nm in diameter. In addition to its incredibly small size, this sp^2 carbon allotrope displayed extreme stability, high tensile strength, high electrical conductivity, high ductility, and high heat conductivity.[19] The unique carbon material later named fullerenes (C_{60}), or buckyballs, gained immense recognition and won both groups, Kroto, Smalley and Curl, the Nobel Prize in 1996. This discovery sparked interest in carbon allotropes over the years that followed, leading to new discoveries among carbon allotropes.

The sp^2 hybridization of carbon, graphite is comprised of multiple carbon sheets, where a singular carbon sheet of graphite is called graphene. Graphene is an atomically thin sheet of carbon that was discovered by removing flakes of graphite with Scotch tape.[20,19,21] This discovery by Andre Geim and Kostya Novoselov in 2004

won them the Nobel Prize in 2010. Ever since, graphene has gained massive recognition because of its outstanding mechanical properties and versatility. Graphene is upwards of 400 times stronger than steel, an exceptional feat for a 2-D, atomically thin material. Additionally, it is also 10 times more electrically conductive than copper, while transparent and very flexible, making it a great candidate for bulletproof vests, drug delivery, biosensors, and flexible screens, etc.[22] Additional carbon allotropes, such as carbon nanotubes are also derivatives of sp^2 carbon.

Carbon nanotubes (CNT's) are extremely lightweight, highly electrically conductive, and very stable structures. The properties of CNT's can be utilized for ultra-lightweight batteries, high-performance plastics, and even medical implants.[23] Additionally, CNT's are extremely strong structures with a tensile strength 100 times stronger than steel. To put in perspective, a simple coating of CNT's on a ceramic scaffold can allow the scaffold to bear 100,000 times its own weight. The principle behind CNT is similar to the use of tightly bound, lightweight bamboo for buildings, however applied on the nanoscale.[23] Each carbon allotrope contains its own set of unique properties that produce a blend of extreme strength, high electrical conductivity, flexibility, and ultimate atomic thinness. These blends of properties are why carbon allotropes are on the frontier of huge scientific advancements.

However, the simplest sp^1, hybridized carbon allotrope remains elusive and impossible to synthesize and isolate. Particular interest in carbyne arises from its potential to exceed the exceptional qualities already seen among carbon allotropes. Carbyne is expected to be 600 times stronger than steel, replacing graphene as the

strongest material.[24] Predictions on the materials properties have embellished significant attention in finding a method for synthesis.

Each carbon atom of carbyne contains two sigma and two pi bonds, capable of yielding two different forms of carbyne. The first is an acetylenic form with alternating single and triple bonds, and the second a cumulenic form with continuous double bonds. Cumulenic carbyne is expected to primarily form, however as carbon chain length increases, it becomes unstable and undergoes a Peierls transition.[25,26,27] Peierls theory states that a 1-D, equally spaced chain with an electron per ion is unstable. To stabilize, carbyne takes on the alternating single and triple bond structure. It is uncertain whether this theory is true, since carbyne synthesis remains unsuccessful.

The first attempt to synthesize sp^1 carbyne was by Adolf von Baeyer, in 1885, who stated that carbyne would forever remain elusive, as its high reactivity would always lead to its immediate destruction. Baeyer also referred to the linear carbon as "explosive diamond".[28] In the case that carbyne is successfully synthesized and condensed, it would be explosively reactive, due to the unpaired electrons found at each end of the chain resulting in rapid polymerization or cross-linking.[29] Experimental evidence of carbon chain bundles has been observed in certain cases, where they are seen encased within carbon nanotubes, or in supersonic-beam-deposited carbon films, and on gold/silver nanoparticle films.[28,25,30] Yet, attempts to physically isolate these carbon chains prove unsuccessful.

However, throughout the numerous attempts to synthesize carbyne, the concept for alternate carbon chains structures has been ignored. The development of stable carbon chains with additional constituents and stabilizers has not been fully investigated and exhibits the potential to harness properties similar to those of

carbyne. The motivation for the work presented in this thesis is to successfully synthesize and characterize new approaches to assemble 1-D carbon structures.

1.3 PSEUDOCARBYNE PROPERTIES

"Pseudocarbyne" is a term coined for 1-D, sp^1 hybridized, carbon chain structures with the inclusion of stabilizing components that carry a resemblance to carbyne and harness similar unique properties. Unlike carbyne, pseudocarbyne does not fall under the classification of a carbon allotrope, since it is not purely composed of carbon. The experimental process implemented for synthesizing pseudocarbyne involves the use of gold nanoparticles to passivate and stabilize the carbon chains. Computational results suggest gold nanoparticles act as stabilizing agents during the formation of pseudocarbyne, by adsorbing onto the surface.[29]

Various measurements can define physical and mechanical properties of materials; including its strength, hardness, stiffness, etc. The strength of a material is typically expressed by its tensile strength. Tensile strength is defined as the maximum point of elastic deformation a material can undergo while still revert back to its original form once the load is removed. The elastic linear deformation is represented by the ratio of stress vs. strain the material endures, and defines a material's stiffness by it's Young's modulus. In Hooke's equation (EQ1.1), the Young's modulus represents a material's resistance to elastic deformation. Permanent, or plastic, deformation occurs when a tensile load surpasses the maximum for elastic deformation, causing the material to rupture. The stress value at rupture point is known as the materials ultimate tensile strength.

$$\sigma = Y\varepsilon, \tag{1.1}$$

In equation 1.1, ε is strain, and σ is stress, and Y is Young's modulus.

Similar to the Young's modulus, the shear modulus defines the elasticity for twisting or torsion force over the material's surface area, and is calculated using EQ1.2.

$$\tau = \frac{F}{A_0}, \tag{1.2}$$

In equation 1.2, F is force, A_0 is surface area, and τ is shear modulus.

In the case of nanosized carbon chains, atomistic quantities need to be implemented.[25] The Young's modulus can be determined by using EQ1.3 and shear modulus with EQ1.4, which follow the same principles seen in EQ1.1 and EQ1.2.

$$\frac{1}{L^2}\frac{\partial^2 E}{\partial \varepsilon^2} = \frac{\pi r^2 Y}{L} \tag{1.3}$$

$$L\frac{\partial^2 E}{\partial \theta^2} = \frac{1}{2} G\pi r^4, \tag{1.4}$$

In equation 1.3 and equation 1.4, E is strain energy per two carbon atoms, and ε is strain, G is shear modulus, L is length of rod, r is atomic radius, θ is torsion angle, and Y is Young's modulus.

When a material is stretched it tends to expand in the same (parallel) direction of force, observed when stretching a rubber band. The displacement and strain on the x-axis over strain along the z-axis represents Poisson's ratio. Incorporating values for shear modulus and Young's modulus into EQ1.5 can solve for the unitless Poisson's ratio.

$$n = \frac{Y}{2G} - 1, \tag{1.5}$$

In equation 1.5, n is Poisson ratio, G is shear modulus, and Y is Young's modulus.

A comparison of materials with prominent mechanical and electrical properties is presented below in Table 1.1, where steel is used as a reference value. Steel is the most extensively used metal material in the world. Its relatively high strength and low production cost makes it ideal for use in transportation, construction, energy, packaging, and appliances. However, with new technology on the rise, the need for better mechanical and electrical properties is growing. Carbon allotropes, such as graphene and CNT's incorporate properties that surpass those seen in bulk metals or materials.

Carbyne is predicted to have tensile strength double that of graphene, while displaying semiconductor properties, and tunable flexibility, within an atomically small chain. Pseudocarbyne is expected to approach similar properties to that of carbyne, with added tunability depending on additional components. The motivation for pseudocarbyne synthesis is to generate a carbon material that features the same exceptional properties of carbyne with added stability and enhancement from gold nanoparticles. The potential in pseudocarbyne lies in applications for nanomechanical systems, optoelectronics, and in areas where strong lightweight materials are required.

Table 1.1: Mechanical Properties of Carbon Allotropes in Comparison to Steel

Material	Tensile Strength	Young's Modulus	Poisson's Ratio	Electric Resistivity	Hardness	Shear Modulus
	MPa	GPa		Ω·m	MPa	GPa
Steel	450	210	0.29	1.43×10^{-9}	1.7×10^{3}	80
Diamond	2.9×10^{3}	1.2×10^{3}	0.22	10^{11}–10^{18}	4×10^{3}	470
Graphene	130×10^{3}	1.0×10^{3}	0.31	10×10^{-9}	5.6	280
Carbyne	251×10^{3}	32.71×10^{3}	-0.65			47.2×10^{3}

1.4 OUTLINE

The information above was provided to give an underlying understanding of the term "pseudocarbyne", and to give insight on the motivation for this research. The focus of this dissertation is on acetylenic carbon synthesis via pulsed laser ablation in liquid. The research centers on varying experimental conditions and the influence they bear on final products. Experimental conditions are laid out in Chapter 2, which describes the different instruments and environmental conditions utilized for synthesis. The techniques used to characterize and analyze samples are explained in Chapter 3. Final results and data comparisons are reviewed in Chapter 4. Future work and concluding remarks are discussed in Chapter 5

.

Chapter 2

EXPERIMENTAL TECHNIQUE

2.1 LASER BACKGROUND

During the 1960's when Theodore Maiman introduced the first laser, scientists did not fully grasp the potential and magnitude this invention would someday have. While the start of laser application began as barcode scanners in 1974, today we see lasers administered in countless applications throughout research labs, dentistry, esthetics, and medical applications.[31] Thanks to Theodore Maiman, the laser certainly solved many unforeseen problems and exceeded expectations becoming arguably the most important tool within the scientific community.[32]

The word "laser" is an acronym for Light Amplification by Stimulated Emission of Radiation. Lasers are very unique light sources that have distinct characteristics. The output beam of a laser is singularly directional (spreads very little with distance), coherent, and typically monochromatic. Contrast to other light sources, which emit light in all directions, a laser requires emitted photons to be identical in phase and direction.[33] Common household flashlights emit incoherent photons in all directions, illuminating their surroundings. The difference between in-phase photons and out-of-phase photons is shown in Figure 2.1.

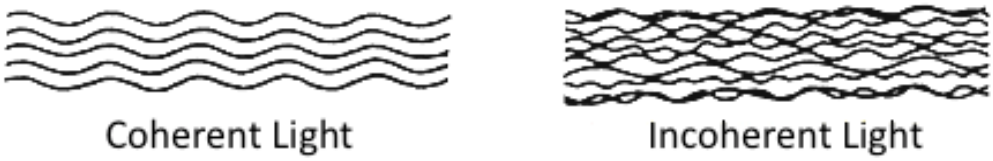

Figure 2.1: A comparison of (left) in-phase, coherent waves emitted from a laser, and (right) out-of-phase, incoherent waves emitted from a flashlight.

Lasers rely on the quantum nature of light. Light and matter interactions occur within the atomic or molecular structure of materials. Each electron on an atom occupies distinct orbitals (s, p, d, etc.) that determine the energy of the electron. The energy level of the atom is highly dependent on the distribution of electrons and their orbitals. These determine whether the atom is in a ground state (lowest energy level) or an excited state (higher energy level). The transitions between different energy levels are shown in Figure 2.2, and occur by three processes: absorption, spontaneous emission, and stimulated emission.[34]

Higher energy transitions can be caused by collisions with free electrons or excited atoms, and by photon interaction. To excite an atom from the ground state to an excited state, the incident photon will need to possess energy equal to the difference in energy levels, shown in EQ2.1.

$$E_2 - E_1 = h\upsilon, \tag{2.1}$$

In equation 2.1, E_1 is the initial lower level energy, E_2 is higher-level energy, h is Planck's constant, and v is the frequency of the light.

The frequency can be defined in EQ2.2 as speed of light divided by wavelength.

$$\upsilon = \frac{c}{\lambda}, \tag{2.2}$$

In equation 2.2, c is speed of light ($8x10^3$m/s), λ is wavelength, and v is frequency.

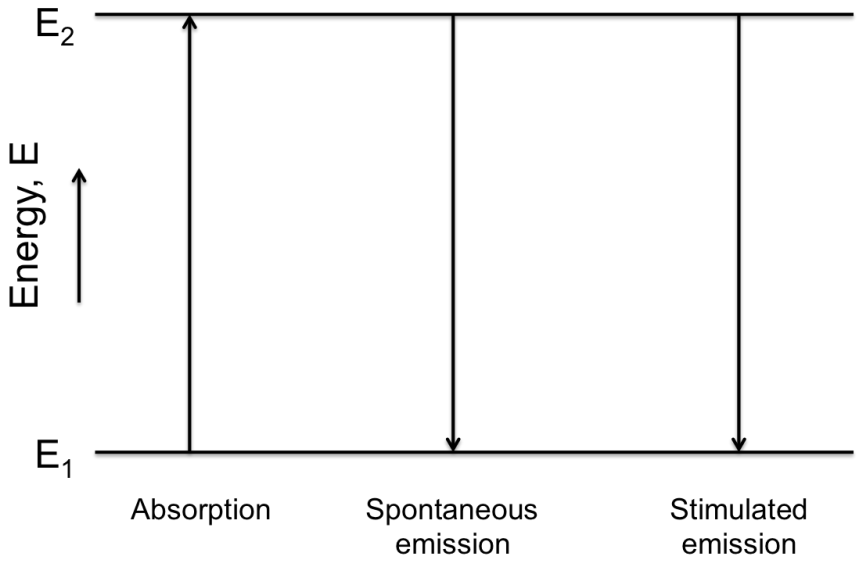

Figure 2.2: Induced absorption occurs when electrons are excited from a low energy level, E_1 to a high energy level E_2. Spontaneous emission releases a photon when an electron relaxes to a low energy level. The photon has energy equal to the difference in energy levels. Induced emission is stimulated by an exterior frequency to emit a photon coherent with the incident photon. The rate of induced absorption is equal to the rate of induced emission.

The same goes for an excited atom at a high energy level, E_2 decaying to a low energy level, E_1 with no outside mechanism. The energy difference remains the same, spontaneously emitting a photon with energy hν, shown in EQ2.3.

$$M^* \rightarrow M + h\nu, \tag{2.3}$$

In equation 2.3, M^* is the excited energy level, M is the ground state, h is Planck's constant, and v is the frequency of the photon.

Photons emitted through spontaneous decay (also known as fluorescence or phosphorescence) have no definite relationship with one another. To emit photons with the same frequency, phase, and direction, emission needs to be induced. Stimulated emission occurs when a photon of specific frequency interacts with an electron in the excited state, causing a photon to be emitted coherent to the incident photon. Unlike spontaneous emission, stimulated emission requires outside radiation to induce emission, laid out by EQ2.4.

$$M^* + h\nu \rightarrow M + 2h\nu \tag{2.4}$$

In equation 2.4, M^* is the excited energy level, M is the ground state, h is Planck's constant, and v is the frequency of the photon.

Lasers require a population inversion of the system to take place in order to operate. Population inversion exists within a system when the number of atoms in the excited state exceeds the number of atoms in the ground state. At any thermal equilibrium, the population distribution within the two states can be determined by the Boltzmann equation (EQ2.5), with most atoms occupying the lower state.

$$\frac{N_2}{N_1} = \frac{g_2}{g_1} \exp - \left(\frac{E_2 - E_1}{kT}\right), \tag{2.5}$$

In equation 2.5, g_n represents the degeneracy of the n_{th} state, k is the Boltzmann constant, N is the population, and T is temperature.

While rising temperatures can drive more atoms towards the excited state, N_2, an increase in temperature can never result in population inversion. This is because an incoming photon has equal probability of transferring the atom to the excited or ground state, and therefore cannot be used to optically pump a two level

system into population inversion. At best, when temperature rises infinitely, $T = \infty$, the population of both energy levels are equal to one another, $N_1=N_2$. To shift the population in favor of the excited state, a system with three or more energy levels, as shown in Figure 2.3, needs to be employed. In a three-level system, E_2 is considered a meta-stable state and E_3 a pump state, where $E_3 > E_2 > E_1$ in energy. Electrons excited to the higher energy level, E_3, are unstable and maintain a short lifetime quickly falling to the metastable level, E_2, where they remain for a longer period of time. This process results in a larger population at E_2 compared to E_1, achieving population inversion. The Ruby laser, discovered by Theodore Maiman, was the first successful three-level laser.[35] Due to the fast energy transition in a three-level system, the electrons in the E_2 energy level still deplete too fast, requiring over half of the atoms in ground state to be excited before attaining inversion. To increase lasing efficiency, most present day lasers, incorporate a four-level energy system.

Similar to a three-level system, a four-level system excites an atom from E_1 to E_4, followed by an almost immediate decay to E_3. In the Nd:YAG laser, the electrons only last in the E_4 level for about 200μs, before they relax to the metastable state, increasing the E_3 levels' population. Since the transition from E_2 to E_1 is fast, the population in E_3 becomes significantly larger than that of E_2, establishing a population inversion within the system. When photons collide with the excited, E_3 electrons, a coherent photon is emitted, and electrons relax to E_2. Afterwards, the population in E_2 quickly decays to E_1 and regenerates the thermal population. In pulsed laser systems, population inversion takes place, by a high-intensity light source in the active medium.

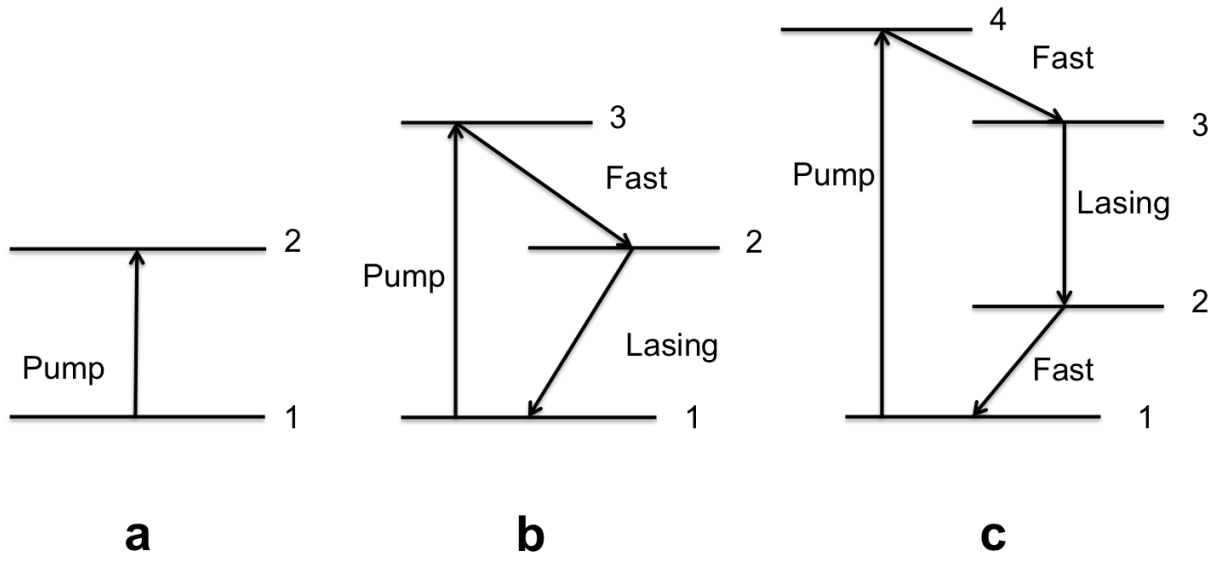

Figure 2.3: Three energy diagrams for (a) two-level (b) three-level (c) four-level transition schemes. The (a) two level transitions scheme cannot achieve population inversion and at best the population in E_1 is equal to the population in E_2. The (b) three-level transition scheme can achieve population inversion with the addition of a metastable state. The (c) four-level transition scheme is the most efficient pumping method for achieving population inversion and is commonly seen among Nd:YAG laser systems.

A very common and well-understood laser, the neodymium-doped yttrium aluminum garnet (Nd:YAG), utilizes four xenon flash lamps, firing for 200μs, as the light source to excite the active medium and obtain a high photon flux over a short period of time. This transfer of energy to the system is called optical pumping. Optical pumping of the neodymium medium generates a lasing activity in the crystal and emits a wavelength of 1064nm in the near infrared region. Every time the lamp flashes, a pulse of laser light is emitted with long pulse durations, producing low peak power. Peak power is highly dependent of pulse width, as seen in EQ2.6, and can be dramatically increased by incorporating an electro-optic device (Q-switch) in the laser cavity to produce shorter pulse durations. The Q switch serves to hold off the lasing, and therefore allows a full population to be initiated before the light is

emitted. Without the Q-switch the atoms are depleted almost as fast as they are excited and therefore limits the efficiency of the gain medium.

$$P_{peak} = \frac{E_{pulse}}{t_{pulse}}, \tag{2.6}$$

In equation 2.6, E_{pulse} is pulse energy, P_{peak} is peak power, and t_{pulse} is pulse width.

A Q-switch is an electronically timed electric pulse on a crystal. It works with the polarizer that is within the laser cavity. The Q-switch can permit or block oscillation between the cavity mirrors to take place. Closing the Q-switch creates a high-loss state, where accumulation of neodymium ion population builds, establishing maximum population inversion. Opening the Q-switch (low loss state) releasing the accumulated energy in the form of a short-pulse, high intensity light.

The Nd:YAG laser uses a potassium dideuterium phosphate (KD*P) crystal for frequency doubling. Due to Q-switching, peak power of each pulse is ample enough to generate non-linear wavelength conversions into second, third, or fourth harmonics at 532nm, 355nm, and 266nm within a nonlinear optical crystal. Since the Q-switch is electronically driven, the operation and ultimate pulse duration is limited to nanosecond timescales to achieve a second harmonic generation; the fundamental 1064nm wavelength is multiplied. Two photons with the same frequency interact with the nonlinear crystal and are combined to form a new photon with twice the frequency at half the wavelength. Q-switched lasers are often used in applications that require high laser intensities in nanosecond pulses.

2.2 PULSED LASER ABLATION IN LIQUID (PLAL)

The theorized phase diagram shown in Figure 2.4 predicts sp^1 carbon forms under high temperatures, ranging from 2600–3800K, and pressures of 10^4–10^9 Pa. [16,17] The feasibility of creating a large scale environment with temperatures reaching that of the surface of the sun is extremely difficult. For the purpose of reaching these extreme conditions, attempts to synthesize pseudocarbyne were carried out by pulsed laser ablation in liquid (PLAL). This technique is capable of confining the high temperature required for synthesis, onto a small (1-2mm) area.

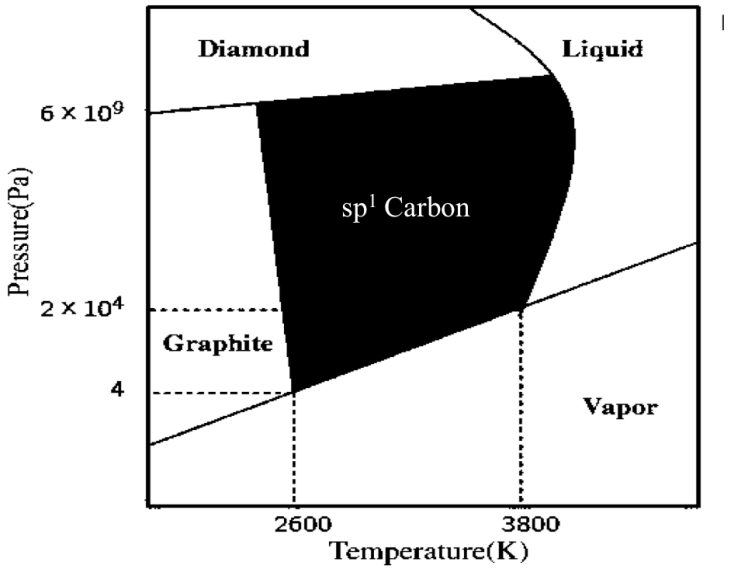

Figure 2.4: Pressure vs. temperature phase diagram for carbon. Graphite is stable under low pressure and low temperature conditions. Diamond forms under high pressure but low temperature conditions. Carbyne is theorized to form under high pressure and high temperature conditions, below melting and boiling points. Reprinted from [16]

The PLAL method focuses a high-power laser beam onto a bulk target generating a localized high temperature and pressure. This localized area involves unexplored chemical reactions that can only occur under extreme conditions.

Combinations of different laser parameters can drastically impact the localized temperature and pressure. To increase odds of carbon chain reproduction, a firm understanding of how these variances affect the thermodynamics of the reaction is vital. Lasers with different timescales, such as, femtosecond, picosecond, nanosecond, etc can be used for synthesis. However, nanosecond lasers tend to be the power source of choice for ablation purposes, offering high productivity and high power at moderate repetition rates, without the cost of an ultrafast laser.

PLAL is considered an alternative laser-based synthesis technique, commonly used for pure nanoparticles generation, free of ligands or adsorbed chemicals. Common synthesis techniques such as chemical reduction methods require chemical precursors that lead to toxic substances or by-products in the samples. To further complicate the synthesis, these processes require many time-consuming steps and costly follow-up treatments for cleaning. Unlike traditional synthesis methods, the single use of a laser in PLAL offers a green solution for synthesizing materials by reducing energy costs and waste treatments, since the only additional items needed are a target material and liquid environment.[31] However, the target material and liquid are extremely important features that constitute the molecular structure of final products.

Gold was chosen as the bulk target and ethanol as the liquid medium for several reasons. The fundamental structure of pseudocarbyne was considered when choosing a liquid medium. Ethanol's (C_2H_6O) structure not only provides the fundamental diatomic carbon building block needed to link alternating single and triple bonds, but it also has a high vapor pressure. The volatility of ethanol is extremely convenient in promptly isolating and crystallizing final products. The use of ethanol as the liquid was inspired by previous carbyne synthesis attempts, which

demonstrated other organic solvents, such as methanol, acetone, and propanol solely formed nanoparticles.[17] As for the target material, when bulk gold is ablated by a high-energy power source, nanosized gold is formed, exhibiting quantum properties unlike that of bulk gold. The nanosized gold in the solution can be selectively ionized depending on the wavelength of the laser and act like a catalyst or substrate during synthesis.

A 532nm green laser was the high-energy power source used to ablate the gold surface, generating a localized thermodynamic environment. The laser passes through a focusing lens, which serves to tighten the spatial profile of the laser beam prior to traveling through ethanol and hitting the gold target. When passing through the ethanol, some of the laser energy is absorbed. To avoid high-energy losses in the liquid, it is best to work under defocused conditions for lasers with longer pulse durations (nanoseconds). Non-linear optical effects are also avoided by maintaining a thin liquid layer of 5mm.

Once the laser beam reaches the gold target it begins to heat the surface. The gold surface absorbs the laser's energy for 10ns at a time, or however long the pulse width is, as **Error! Reference source not found.** shows. The optical penetration depth has a direct relationship to the absorption coefficient by EQ2.7.[36]

$$\delta = \frac{1}{\alpha}, \tag{2.7}$$

In equation 2.7, α is absorption coefficient and δ is optical penetration depth. Gold has an absorption coefficient of 5.9431×10^5 cm^{-1},[37] which yields a penetration depth of 16.8 nm according to EQ 2.7.

The electron kinetic energy, absorbed from photons, is converted to thermal energy and heats the gold nanocrystal lattice. The gold heats at a rapid picosecond timescale and undergoes simultaneous thermal processes, such as, vaporization and melting.[38] The system only undergoes thermal processes when nanosecond pulses are used, affecting a larger area than the one defined by the penetration depth, shown in EQ2.8. When femtosecond pulses are used, the system is driven directly to the gas phase without crossing the gas/liquid phase.[38]

$$L_{th} = (2\tau_L \delta)^{\frac{1}{2}}, \tag{2.8}$$

In equation 2.8, δ is thermal diffusivity and τ_L is pulse width.

The gold is unable to absorb the full amount of energy supplied by the laser and releases the excess energy in the form of a shockwave, within 50ns, during which ablation is taking place. A shockwave is a pressure wave travelling in a medium and is caused by the discontinuity of density.[36,38] One shockwave is propagated into the liquid and the other counter propagated into the solid.[38] The energy released into the liquid environment is 10–50% of the energy absorbed by the gold. The supersonic velocity of the shockwave is on the order of 10^3 m/s.

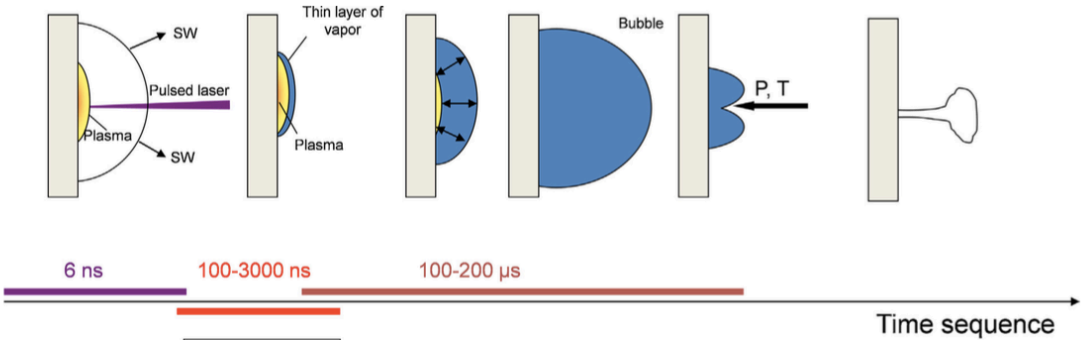

Figure 2.5: Illustration showing a time sequence for PLAL. The process begins with the laser beam striking the target and forming a plasma plume, which expands supersonically, generating a shockwave. Within 200µs, pressure and temperature significantly drop and the cavitation bubble collapses. Reprinted from.[39]

Ablation can occur by three thermodynamic mechanisms, vaporization, normal boiling, and explosive boiling. Typical PLAL is performed with nanosecond pulses, causing material detachment to take place by explosive boiling. Photoionization of the metal particle occurs by a multiphoton process, which causes Coulombic explosion or explosive boiling due to rapid heating to the critical temperature and charge repulsion in the particle. Pulses of longer time cause detachment to occur by vaporization, whereas shorter pulse widths (femtosecond, picosecond) drive the system directly into the gas phase by direct fragmentation.[38]

The plasma contains highly ionized material due to the high temperature and direct photoionization.[38] The formation of non-equilibrium plasma reaches temperatures of 10^3-K, and pressures of 10^{10} Pa. After the 10ns laser pulse the plasma has a tens of nanoseconds lifetime. With nanosecond pulses, the plasma and laser pulses coexist, vaporizing the material even further. As a result, nanosecond pulses lead to better nanoparticle size distribution compared to femtosecond or picosecond ablation. The plasma cools with expansion and heat exchange to the

surrounding liquid and target. However, thermodynamic equilibrium of the plasma is not reached. The energy released from the plasma plume into the surrounding environment initiates the rise of a cavitation bubble: this occurs within 100ns–10μs. The bubble expands at supersonic speeds, $>10^3$m/s. The bubble lifetime is roughly 100μs. During this time, the temperature within the bubble begins to decreases and the pressure inside drops below the pressure of the surrounding liquid. When the bubble collapses, a second shockwave releases nanomaterial into the solvent, shown in Figure 2.6.

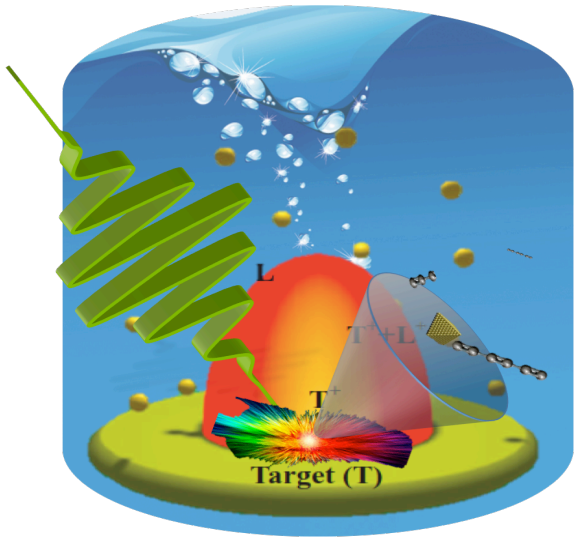

Figure 2.6: Illustration of a gold target submerged in an ethanol beaker. A 532nm laser beam strikes the gold target, transferring heat and generating a localized high temperature, high-pressure area. A plasma plume forms, as a result, and initiates the expansion of a cavitation bubble. When the cavitation bubble collapses, synthesized carbon product and gold nanoparticles are released into the liquid.

The nanomaterial released into the liquid consists of gold nanoparticles and acetylenic carbon chains. The nanoparticles in liquid are ionized and reirradiated as laser ablation continues. The surface of the gold nanoparticle is negatively charged

due to laser ionization. Electrostatic stabilization of the particles is achieved due to partially or fully oxidized surfaces, where ion adsorption takes place and forms an electrostatic double layer. The acetylenic carbon structures also found in the liquid were formed in the cavitation bubble when plasma temperatures quickly declined and reached synthesis conditions.

2.3 LOCALIZED TEMPERATURE AND PRESSURE

Laser-induced plasma is considered a system composed of roughly equal amounts of electrons and ions that interact with one another to give quasi-neutral domains. Since radiation constantly emits energy outside the plasma system, a complete thermodynamic equilibrium is never reached. When collision processes are more dominant than radiative processes for energy transfer, radiation can be neglected. In plasmas produced by ablation with nanosecond-pulses, the temperature is mainly due to the phenomenon of inverse Bremsstrahlung heating, where electron heating is caused by absorption of energy from the laser's electric field, which takes place in the case of long pulses.[40] To determine the localized temperature and pressure, the approximation of local thermodynamic equilibrium (LTE) is used in the case of erosion plasma. This approximation assumes thermodynamic equilibrium exists in a small region of the plasma.

Calculations for LTE depend on the electron-ion relaxation time, which is the time needed for the electron gas to transfer the absorbed laser energy to heavy particles through elastic collisions. After sufficient collisions, the species in the plasma share the same kinetic energy, characterized by a common temperature. The energy of the laser beam is supplied to electrons, meaning electron temperature will always exceed the temperature of heavy particles.[41] The electron temperature is

considered the characteristic temperature of the plasma, since energy transfer is mainly through collisions with electrons.

In a 5W laser with repetition ate of 20Hz, there is 250mJ of pulse energy, with 6.69611×10^{17} photons in the laser beam, all supplied to the gold target. Reflection from the gold target induces energy loss and only 30% of laser energy is absorbed. Before plasma formation, gold melts at a temperature of 1337K with a latent heat of fusion of 63kJ/kg. At a temperature of 3109K, gold begins to vaporize and has a latent heat of vaporization of 330kJ/mol. Additionally, during the formation of plasma; shockwaves are propagated into the solid and liquid leading to more energy losses. Each shockwave emits 10–50% of energy absorbed. Assuming a 35% loss of energy due to the shockwaves, these processes remove 177mJ of energy from the bulk gold target. Incorporating the initial energy into EQ2.9, where losses are incorporated, provides the localized plasma temperature.

$$T(K) = \left(\frac{Q - \Delta H_{fusion} - \Delta H_{vapo\square ization}}{C_p} + 273.15\right)(1 - \mathrm{R})\, S_1 S_2, \tag{2.9}$$

In equation 2.9, C_p is specific heat of gold of 26J/K mol, ΔH_{fusion} is enthalpy of melting, $\Delta H_{vaporization}$ is enthalpy of vaporization, R is reflection loss of 0.7, S_1 is shockwave loss in solid, S_2 is shockwave loss in liquid, and Q is energy.

If the system were to undergo no losses, the plasma would have a temperature of 4.4×10^4K. If only reflection losses were considered, then the plasma temperature would be 1.34×10^4K. Considering losses due to vaporization and melting, the plasma temperature reduces to 8000K. The resulting plasma temperature is 3600–6000K depending on losses due to shockwaves.[36,38] The quick

calculation suggests the temperature conditions theorized to produce carbyne are reached during experiments.

Although the mechanism is not yet known for how ethanol transforms into carbyne-like materials, the experimental atmosphere around the gold is sufficiently hot to atomize the ethanol. The triple point of ethanol is only 1000K, and the crude approximation suggests plasma temperature exceeds 3000K. Thus, it is easily assumed that the ethanol molecules are within the localized high temperature and high-pressure region at the gold's surface and begin to dissociate. The hydrogen atom in the hydroxyl group firsts reacts with active gold nanoparticle ions in the plasma and becomes Au-H intermediates. The gold nanoparticles are theorized to act as catalysts during the reaction and break the bonds between a pair of α-H and ß-H from the ethanol molecule. This break causes the C–C single bonds to become C–C double bonds. The ethanol molecules in the plasma form diatomic carbon with Au-H intermediates and oxygen. The Au-H intermediates react with nucleophiles such as hydroxyl groups or oxygen, removing hydrogen from the gold surface and creating water. This leaves a singular diatomic carbon with a free electron on each end. The diatomic carbon forms cumulenic, double bonded, carbon chains. Due to instability, the carbon chains undergo a Peierls transition and form acetylenic carbon chains, of alternating single and triple bonds.

$$(CH_3OH)_n + Au = (C_2)_n + (HOH)_n + (H_2)_n$$

2.4 EXPERIMENTAL SETUP

Pseudocarbyne synthesis was carried out using the second harmonic produced by a high power Q-switched Nd:YAG laser from Spectra Physics, specifically, the Quanta-RAY PRO250 Pulsed Nd:YAG laser (a wavelength of 532

nm, repetition rate of 20 Hz, and laser pulse width of 10 ns) was utilized to perform PLAL. The laser was focused down with a 15 cm focal lens onto a bulk gold target (99.999%) fixed at the bottom of a beaker. Absolute ethanol was poured into the beaker, with 5mm thickness above the gold target.

Raster Scan

During early stages of the pseudocarbyne synthesis, the beaker system was placed on an x-y translation stage. The translation stage was attached to two motors and was controlled by MatterControl software.[42] The purpose of the translation stage was to prevent holes from being drilled into the gold plate by the high power laser. The translation stage succeeded in raster scanning the gold plate surface and led to an even ablation. The motors used to control the x-y stage constantly needed maintenance and repair, which hindered pseudocarbyne synthesis progress. Eliminating the raster scan did not generate any holes in the gold plate. Further, it was determined that the depth of the gold ablation was not significant during a production, and could be manually adjusted on a day-to-day basis to find fresh surfaces. For this reason, use of the x-y translation stage was discontinued.

Closed System

The initial pseudocarbyne synthesis was attempted in a closed system to remove any concerns of having atmospheric contamination, and to completely prevent oxygen from being present. The enclosed reactions also made for a safer tabletop experimentation and blocked laser light scatter. The closed and open systems were carried out under identical laser parameters. Nitrogen was supplied to

the system and was bubbled through the liquid to purge the oxygen. The chamber used for the closed system was very large and required an excessive amount of liquid to create a 5mm layer of ethanol. Aligning the laser beam proved difficult, as well as, preventing the gold plate from shifting. Most importantly, the stainless-steel chamber was difficult to properly clean and led to contamination of our samples. Use of the enclosed system was terminated, since purging the system of oxygen by nitrogen flux was sufficient.

Open Beaker System

Experiments were conducted in an open beaker system under nitrogen flux to prevent any combustion of the gas. The laser pulse power ranged from 700mW at its lowest to 5W at its maximum, with a spot size of 2mm. Multiple samples underwent short periods of ablation (~15 minutes), while others were ablated for several hours (~13 hours). The laser power and ablation time were varied to discern their effect on final products, presented in chapter 3.

Before performing experimentation, all beakers and equipment are sonicated to remove any contaminants adhered to surfaces. The tabletop laser setup is designed so the beam comes down and ablates the gold surface at ~90º angle. The 50mL beaker contains a fitted, stainless steel platform, devised to situate the gold plate at the bottom of the beaker. The beaker is filled with absolute ethanol until the thickness above the gold plate is roughly 5mm. An aluminum plate with two holes is positioned on top of the beaker. The larger centered hole allows the laser beam to pass through without interference. The smaller hole on the edge is designed to allow nitrogen flow into the system and flood out any remaining oxygen. As a safety

precaution, nitrogen is flown into the beaker for one minute before running experiments to ensure all of the oxygen has been purged. A glass slide is placed on the large center hole of the aluminum plate to prevent any splashing from reaching the focal lens. Together, with the nitrogen, the glass slide prevents any oxygen to be present in the system.

The laser beam is aligned while the laser is running on Long Pulse (LP) mode. It is safer to align in LP mode when the Pockels cell and flash lamps fire simultaneously, emitting a beam of less power. The mode of the beam is checked with thermal sensitive paper and by firing SINGLE SHOT on the controller. After the beam is aligned the controller can be changed to Q-Switch mode. Once the setup is aligned and assembled, orange laser shields, blocking 532nm light are arranged to enclose the system. Proper laser safety requires these shields in conjunction with 532nm shielding laser goggles.

To increase laser power, the oscillator knob is maxed out reaching approximately 1W. Increasing the amplifier allows the system to reach a max power of 7W for 532nm light. A Scientech Mentor MA10 power meter was utilized to attain an ideal power output of 5W. As a laser beam passes through a focal lens, it narrows down to a minimum attainable diameter, or beam waist. The beam diameter at any distance away from the focal lens can be determined by,

$$w_0 = \frac{M^2 \lambda f}{\pi r}, \tag{2.10}$$

In equation 2.10, $M \geq 1$ is a measure of how perfectly Gaussian the mode of the beam is (1.00 is a perfect TEM_{00} beam), f is focal length, and r is unfocused beam radius.

The Rayleigh length in EQ2.11 is used to approximate the distance for which the waist and energy of the beam remain roughly constant.

$$z_r = \frac{\pi w_0^2}{\lambda}, \tag{2.11}$$

In equation 2.11, λ is the wavelength of light (532 nm) is determined to be 152 μm. The beam waist at any given position can be calculated using EQ2.12, where z is the distance away from the focal lens.

$$w(z) = w_0\sqrt{1 + (\frac{z}{z_r})^2}, \tag{2.12}$$

Figure 2.7 shows the beam waist for an initial focus of 15cm. Light cannot focus to an infinitesimal point due to the diffraction limit of light. With a 15cm lens and an initial beam radius of 5mm, a minimum beam diameter of 5.08μm is achieved.

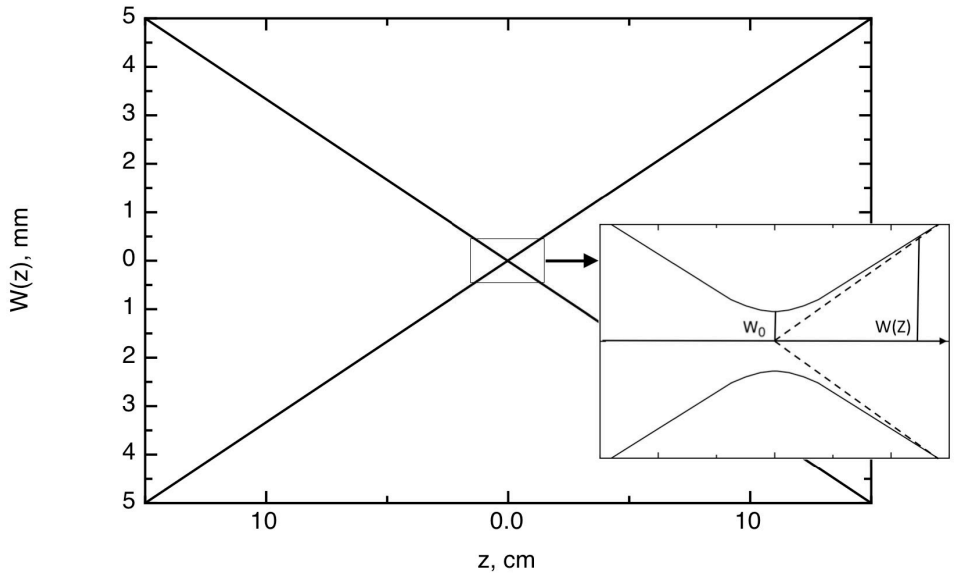

Figure 2.7: The focus of a Gaussian laser beam. The diffraction of light limits the minimum beam radius to a finite value labeled w_0.

A change of focal length can lead to a smaller or larger beam waist. Figure 2.8 shows the beam waist for a 12cm focal lens vs. the 15cm focal lens used for experiments. When the focus is adjusted to 12cm and a radius of 5mm, the beam waist is 4.06μm.

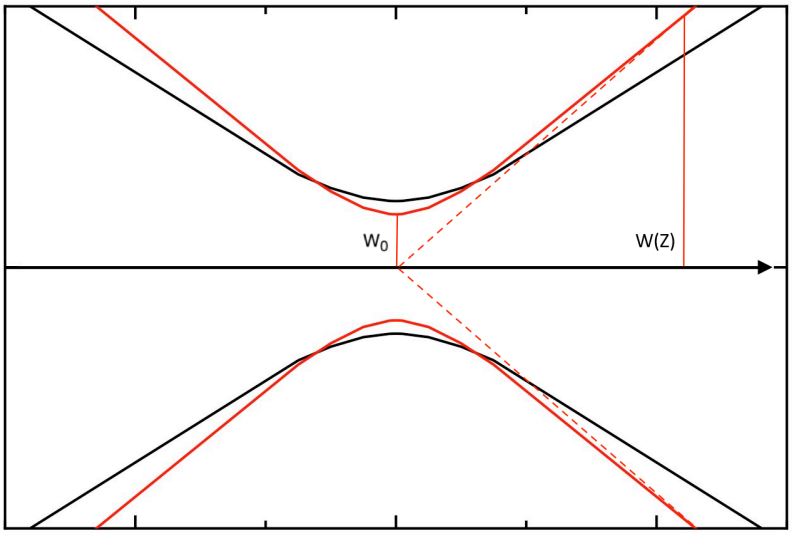

Figure 2.8: The focus of a Gaussian laser beam. The red represents the condition where the focus is 12cm and the black represents 15cm focus. The dashed line shows the focal conditions where the diffraction limit of the laser is ignored. It can be quickly observed that a tighter focal lens produces a smaller focal length.

The synthesis of pseudocarbyne molecules and materials requires careful tuning of the laser parameters and environmental conditions, with final products greatly varying due to laser parameters and environmental conditions, such as, pulse duration, wavelength, energy, and repetition rate.[36] These parameters determine the fluence and intensity the laser is operating at. Fluence is defined as the energy of the laser beam per area as shown in EQ2.13. The intensity is determined by accounting for the laser's pulse width as presented in EQ2.14. In the nanosecond ablation community, it is common to report the fluence of the laser for rapid comparison with other experiments. This is because the common nanosecond laser operates on similar physical principles as described in section 2.1. This is in contrast to other communities; such as the femtosecond excitation community where pulse widths differ greatly and can change the intensity of the laser beam by orders of magnitude.

$$\frac{E_p}{A} = \frac{J}{cm^2} \tag{2.13}$$

$$\frac{E_p}{A\,\tau_p} = \frac{W}{cm^2}, \tag{2.14}$$

In equation 2.13 and equation 2.14, A is focal spot area, E_p is laser pulse energy, and τ_p is pulse width.

During PLAL the laser beam passes through the carbon rich liquid environment prior to reaching the target. The liquid refraction of the linear focused beam will cause the ideal focal length to increase, and can be calculated using EQ2.15.[36] The correction value for the increase in focal length is:

$$\Delta f = l\,(1 - \frac{f}{\sqrt{n^2 f^2 + (n^2-1)r^2}}), \tag{2.15}$$

In equation 2.15, f is focal length of the lens, l is liquid thickness, and n is the refractive index of the liquid (1.3617 for ethanol). [43]

By assuming a liquid thickness of 5 mm, this causes a shift in the focal distance by 0.1cm. This correction achieves a spot size of 1mm with a fluence of 25 J/ cm^2 and an intensity of 2.5 GW/ cm^2. The combination of a 1mm spot size with 5W of power leads to violent splashing caused by optical breakdown, which takes place when ablation conditions are above threshold. The spot size is an important feature that must be accounted for accurate treatment of the ablation and plasma conditions. Literature values state irradiation intensity threshold for nanosecond pulsed laser systems lie between 0.2–1.0 GW/cm^2, where plasma is characterized by high-density effects.[39] To remain within threshold range, the focal lens was translated towards the sample by 3 cm, which unfocused the beam and achieved a

final beam diameter of 2mm. Incorporating the adjusted spot size, the laser fluence for the system was 6.25 J/cm^2 with an intensity of 0.625 GW/cm^2.

The samples produced under various reaction times were compared to optimize the experimental run times. A comparison of the samples revealed that an ideal run time of 2 hours was necessary to produce a significant concentration of materials that could be detected spectroscopically. Ethanol constantly had to be replenished as long run times caused it to evaporate and liquid thickness decreased. Liquid thickness greatly influenced the focal conditions and was watched closely to ensure a uniform thickness was maintained, never exceeding 5mm. A thick layer would cause optical breakdown of the liquid and reduce ablation productivity. At the conclusion of an experimental run, typically around 3mL of liquid remained. The sample was removed from the beaker and placed in an Eppendorf sample container. The final samples were translucent and varied in color that could be related back to experimental conditions such as laser power and ablation time. For example, using a laser power of 5W for over an hour produced dark purple samples. The color of these samples is attributed to the production of nanoscale gold particles in colloidal suspension that are produced as byproducts alongside pseudocarbyne. Over a period of time the nanosized gold lost stability, aggregated, and settled to the bottom as dark purple clumps.

Purification

Following PLAL synthesis, the colorful samples contained a mixture of several components, including gold nanoparticles. The samples undergo a purification process to remove any large or aggregated gold nanoparticles from the

solution. The gold nanoparticles typically settle independently in the solution within minutes or typically over a 24-hour period depending on the concentration of the gold particles. To expedite the separation process, samples were placed in a VWR Galaxy C-1200 Mini Centrifuge and were run at 6000 rpm for 15 minutes. Once this process was complete, the Eppendorf containers left a clear, transparent solution with pelletized gold at the bottom. The clear portion was extracted and placed in a new Eppendorf container.

To further purify samples and extract only product of interest, samples were pumped through a reverse-phase high-performance liquid chromatography (HPLC) column on a waters 600EHPLC system with a phtotodiode array detector (3.0 x 250 mm C-8 column, 5μm particle, 300Å pore, YMC-Pack HPLC) using methanol gradients. HPLC is a packed column technique used for separating various components and bi-products found within the sample. The instrument used for purification utilized a C-8 (Octylsilane) column as the packed bed and sorbent, also called the stationary phase. The mobile phase, methanol, carries the sample through the column. Each component within the sample has different strengths of interaction with the sorbent and mobile phase depending on its chemical nature and polarity. This interaction causes components to move through the column at different rates and therefore allows them to be separated. The amount of time it requires the analyte to emerge from the column is considered its retention time, usually quoted in units of minutes or seconds. In the case of reverse-phase HPLC, the hydrophilic components will have a lower retention time than hydrophilic components.[44] Retention characteristics of the analyte will be affected depending on its ionization state. The hydrophobicity of a molecule is the primary indicator to its retentivity. The hydrophobicity of a molecule can be calculated by using EQ2.16

below, where the hydrophobicity is a measure of the way an analyte (neutral) partitions between two immiscible solvents (methanol and water).

$$logP_{meth/water} = \log\left(\frac{solute_{meth}}{solute_{un-ionised\ water)}}\right) \quad (2.16)$$

Retention time increases when the number of carbon atoms increases. Additionally, straight chain hydrocarbons also have higher retention time than analytes with functional groups.[44] The emerging products are detected with a dedicated UV/Vis spectrometer that analyzes the samples at a frequency of 1Hz, and makes it is possible to collect the purified samples while discarding the rest of the liquid. This technique is used to concentrate and purify the materials of interest.

Chapter 3

TECHNIQUES FOR CHARACTERIZATION

3.1 ROVIBRATIONAL & ELECTRONIC ENERGIES

Light and matter interact in a number of different ways. As Figure 3.1 shows, a molecule or material can interact by scattering, reflecting, absorbing, or transmitting light. Since the type of interaction depends on the composition of material and wavelength of light, it can be utilized to identify and characterize unknown molecules.

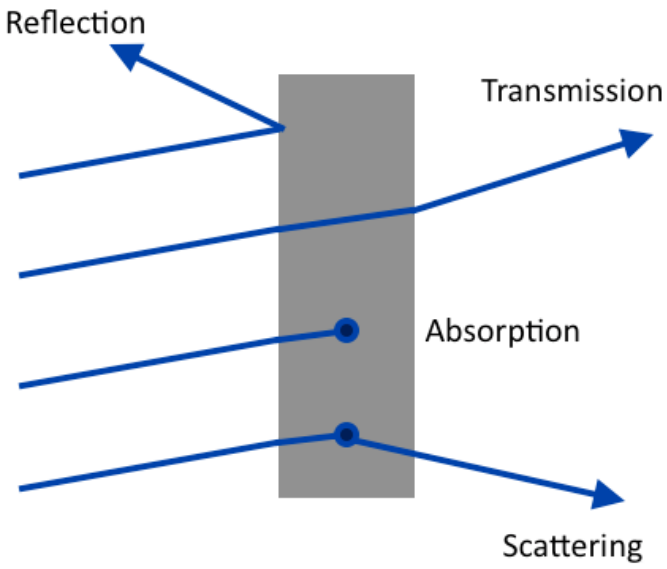

Figure 3.1: Diagram of different light and matter interactions: reflection, transmission, absorption, and scattering. Modified from [45]

Molecules have three types of degrees of freedom (DOF) that describe its movement. In total there are 3N degrees of freedom, where N is the number of atoms in the molecule. The three types of DOF are translational, rotational, and vibrational. The simplest form is translational, which only entails movement of the

molecules center of mass and is described by three orthogonal vectors. Each orthogonal vector produces one DOF, with a total of three DOF. Rotational DOF are described as rotations around the molecule's center of mass, where three vectors represent the moments of inertia. In the case of a linear molecule only two DOF are present due to negligible inertia from rotation along the bonds.

Diatomic molecules are modeled as a rigid rotor. The rotational energy in, EQ3.1, is determined assuming two masses are attached to each other with a fixed distance.

$$E_{rot} = \frac{h^2}{8\pi^2 I} J(J+1) = BJ(J+1) \tag{3.1}$$

$$I = \mu r^2 \tag{3.2}$$

$$\mu = \frac{m_1 m_2}{m_1 + m_2}, \tag{3.3}$$

In equation 3.1, equation 3.2, and equation3.3, B is the rotational constant, h is the Planck constant, I is moment of inertia, J is the rotational quantum number, m_1 and m_2 are the atom masses, μ is the reduced mass, and r is the equilibrium bond length.

The energy of the transitions must be equivalent to the energy of the photon of light absorbed. The difference in energy between rotational levels is on the order of $10cm^{-1}$; microwave region. These equations for rotational transitions exclude distortion corrections caused by centrifugal forces.

A molecule's rotation is affected by its vibrational transition due to a change in bond length causing rotational levels to be superimposed within vibrational levels. Vibrational DOF are the total DOF minus the translational and rotational and are determined by 3N-6 for nonlinear molecules and 3N-5 for linear molecules. Vibrations are caused by internal movements of the molecule and arise from

combinations of bending, stretching, and contractions that occur between bonds. Vibrational transitions can be approximated and are modeled by use of a harmonic oscillator. The harmonic oscillator contains constant energy spacing and approximates molecules as being two-point masses connected by a spring with an equilibrium distance, r_e. The harmonic oscillator approximation works best for low energy transitions. Vibrational transition states occur on the order of $1000cm^{-1}$. The vibrational energy for a diatomic molecule modeled by a harmonic oscillator is:

$$E_{vib} = hv_e\left(\upsilon + \frac{1}{2}\right) \tag{3.4}$$

$$v_e = \frac{1}{2\pi}\sqrt{\frac{k}{\mu}}, \tag{3.5}$$

In equation 3.4 and equation 3.5, h is the Planck constant, k is the spring constant, μ is the reduced mass, v_e is the vibrational frequency, v is the vibrational quantum number.

Vibrational spectroscopy can be used to assign the chemical structure of a molecule. Certain energies in the visible spectrum can be attributed to specific vibrational stretches or bends. For a vibration to be observed through traditional absorption spectroscopy, a vibration must cause a change in the dipole moment of the molecule. An alternative spectroscopic technique can be used to observe the vibrational modes that exhibit a change in polarization, known as Raman spectroscopy. A vibrational mode can be IR active if it has the same symmetry as a component of the electric dipole vector: x, y, or z. A Raman active vibrational mode has the same symmetry as a component of the molecular polarizability: x^2, y^2, z^2, xy, yz, xz, etc. These vibrational signatures can be used as a fingerprint to understand a molecule's structure.

Electronic transitions involve the absorption of light to bring the molecule to an excited electronic state. At equilibrium, the molecule is in a ground electronic state, typically v = 0. To reach a higher electronic state, spin must be preserved and parity has to change. According to the Franck-Condon Principle, electrons move and respond much faster than nuclear motion. As a result, excitation has no effect on nuclear geometry. Electronic transitions require a large amount of energy and can often break bonds. A molecule can be excited to a binding or dissociative state. The unbound state will cause the molecule to dissociate into atoms. Whereas, excitation from v' = 0 ground to v" = 2 excited state will relax non-radiatively to a stable minimum of v" = 0. At v" = 0 there is a large amount of energy to be released to the ground state. This release of energy can be measured as fluorescence.

Electronic, vibrational, and rotational energies all have contributions that scale with the electron to nucleus ratio. These energies can be correlated as such:

$$E_{elec}: E_{vib}: E_{rot} \sim 1 : \sqrt{\frac{m}{\mu}} : \left(\frac{m}{\mu}\right), \tag{3.6}$$

In equation 3.6, m is the electron mass and μ is reduced mass.

3.2 UV/VIS

UV/Vis spectroscopy is a simple and inexpensive way to determine the concentrations within a solution. During UV/Vis, a wavelength in the range of 190nm–1100nm is passed through a cuvette containing solution. When molecules are exposed to light with energy that matches a possible electronic transition within the molecule, some of the light energy will be absorbed as the electron occupies a higher energy orbital. The amount of light absorbed is dependent on the sample

concentration, the path length of light through the cuvette, and the wavelength absorbed. The transmittance (I/I_0) indicates the concentration within your sample. When transmittance is 100% it indicates no light is absorbed by the sample. Absorbance can be calculated using EQ3.7.

$$A = -\log_{10} T = -\log_{10} \left(I/I_o\right), \tag{3.7}$$

In equation 3.7, A is absorbance, I is incident light out, I_o is incident light in, and T is transmittance.

The absorbance of a sample can be correlated to concentration by EQ3.8 to produce the Lambert-Beer law seen in EQ3.9.

$$I = I_o\, 10^{-(\varepsilon l c)} \tag{3.8}$$

$$A = \varepsilon l c, \tag{3.9}$$

In equation 3.8 and equation 3.9, c is concentration, ε is molar absorption coefficient, and l is path length through cuvette.

The resulting spectrum is shown as a graph of absorbance vs. wavelength. When UV (200–380nm) or visible light (380–780nm) is absorbed, an electronic transition takes place between the frontier orbitals. The energy supplied from the light excites electrons from their ground state orbitals to higher energy orbitals, shown in Figure 3.2. Three types of ground state orbitals exist, σ–bonding, π–bonding, and non-bonding. The ground state can transition to two anti-bonding orbitals, σ*, and π*, where shorter wavelengths require greater photon energy. As a result, the σ→σ* and n→σ* transitions require a great deal of energy and only occur

in the far ultraviolet region (<150nm). On the other hand, π→π* and n→π* absorb longer wavelengths and require less energy.

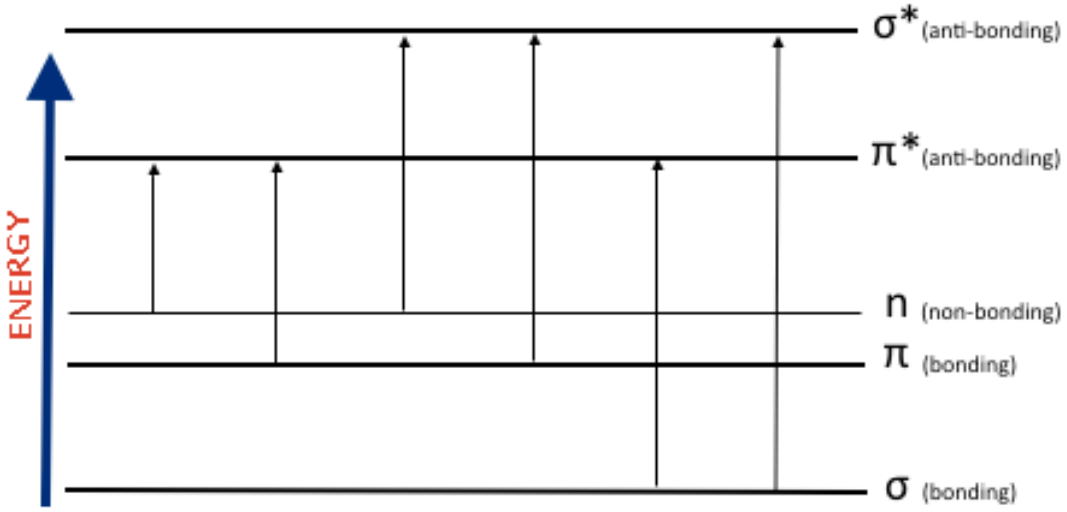

Figure 3.2: Diagram showing electronic excitation levels. Transitions between σ→σ* and n→σ* require more energy and absorb shorter wavelengths.

Considering electronic transitions among carbon structures, a σ→σ* transition is seen for C–C or C–H with sigma bonded electrons.[46] The pi bonded electrons of C–C double and triple bonds have π→π* transitions with absorption peaks near 200nm. The lowest energy n→π* transition also absorbs near 200nm.

Localized Surface Plasmon Resonance (LSPR)

Gold nanoparticles have a large number of easily polarizable conduction electrons surrounding its spherical core. The intense response of gold nanoparticles to electromagnetic excitation is largely due to the localized surface plasmon resonance (LSPR). Plasmons are a coherent oscillation of the surrounding free

electrons with respect to the atomic nuclei.[6] The plasmon can be viewed as a mass-spring oscillator, where the electron cloud oscillates like a simple dipole, parallel to the electric field. Only a well-defined frequency in resonance with the oscillation can excite LSPR.[6] The LSPR of gold nanoparticles falls between 520-600nm on the absorption spectrum, because of this, a green 532nm laser can re-irradiate the gold nanoparticles and excite their LSPR. This phenomenon causes gold nanoparticles to act like nano-antennas and produce electric fields that are orders of magnitude larger than the driving laser field.[47] This selectively heats and ionizes the gold allowing them to act as catalysts during synthesis.[6,48] The LSPR can change by varying a particles size and shape.

The diameter dependence of LSPR is due to both intrinsic confinement and extrinsic effects.[49] For nanoparticles smaller than the wavelength of light, a uniform electric field distribution along the particle is present when the size parameter $x \ll 1$. This is typically the case for gold nanoparticles of 25nm in diameter or smaller.

$$x = {}^{\pi d}/_{\lambda}, \tag{3.13}$$

In equation 3.13, d is nanoparticle diameter, λ is incident wavelength, and x is size parameter.

The extrinsic effect is caused by the non-uniformity of the electric field inside nanoparticles. This causes a retardation effect due to incoherent multipolar plasmon modes, which arises from an increase in nanoparticles size. The extrinsic effect is seen on the absorption spectrum as broadening and red shift to longer wavelengths of the SPR as particle size increases. Retardation effects are dominant in particles 60nm of larger.

The intrinsic confinement inhibits the dielectric function of metal resulting from the finite size of the gold nanoparticle. This intrinsic confinement occurs for nanoparticles with a radius smaller than the mean free path of the conduction electrons, approximately 30nm for gold. The result is a dampened LSPR band for very small particles. The LSPR band is almost completely diminished for particles smaller than 2nm.[10]

Different shapes for gold nanoparticles also exist revealing different characteristics. Gold nanorods are shown to have a transverse (short axis) and longitudinal (long axis) LSPR band. The LSPR band is dependent on electron oscillations parallel and perpendicular to the rod length. The transverse LSPR is similar to those of gold nanospheres with and absorption peak around 500nm. The longitudinal LSPR band is tunable from the visible to near-infrared spectrum (797nm).

Mie Theory

Due to their small size and high surface-to-volume ratio, gold nanoparticles exhibit nonlinear optical properties, described by Mie theory.[49] The collective oscillation of the conduction electrons is what gives colloidal solutions a distinct color. LSPR excitation of the gold nanoparticles is responsible for the pronounced peaks observed in the optical absorption or extinction spectra, unique to particle size.

UV/Vis spectroscopy measures the extinction cross section of a molecule between the ground state and the excited state. The extinction is the sum of scattered and absorbed photons, and is proportionally dependent on particle size.

$$\sigma_{Ext} = \sigma_{Abs} + \sigma_{Sca} \tag{3.10}$$

The extinction cross section can be related to measured transmittance (EQ3.11) and absorbance (EQ3.12)

$$T = \frac{I}{I_o} = \exp\left(-l \frac{N}{V} \sigma_{Ext}\right) \tag{3.11}$$

$$A = -\log_{10}\left(\exp\left(-l \frac{N}{V} \sigma_{Ext}\right)\right), \tag{3.12}$$

In equation 3.11 and equation 3,12, I is incident light out, I_o is incident light in, l is path length, N is number of particles, and V is volume.

The cross section for absorption dominates over the cross section for scattering when the diameter of a nanoparticles is significantly smaller than the wavelength of excitation light.[6] When this occurs, the cross section for extinction becomes comparable to the cross section for absorption. Figure 3.3 represents the LSPR band for gold nanoparticles that are 10nm in diameter. The absorption peak is centered on 525nm and was generated using Python code solving for Mie theory.[50] The peak center shifts depending on nanoparticle size.

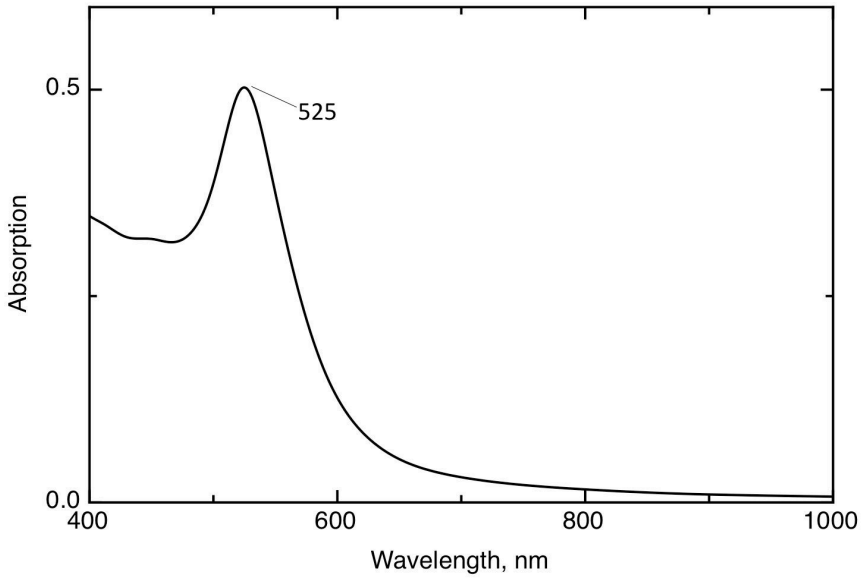

Figure 3.3: LSPR absorption peak near 525nm is common for gold nanoparticles. This plot is generated for nanoparticles that are 10nm in diameter

For larger particles, still smaller than the wavelength of light, the cross section for scattering scaled with r^6 of the particle. Both absorption and scattering effects become comparable at around 50nm for gold nanoparticles. Once particles surpass a diameter of 70-100nm, scattering effects dominate.[6] The scattering effect is beneficial in medical fields as a tool for biolabeling and sensing. On the other hand, absorption effects involve the transfer of a photon to the nanoparticle, where it is converted to heat. Absorption effects of nanoparticles are incorporated in cancer treatments where they optically heat and ablate tumors. [6]

3.3 RAMAN SPECTROSCOPY

Raman spectroscopy centers on the inelastic scattering of light and the resulting molecular vibrations to identify unknown materials. This technique works by irradiating a sample with a monochromatic light source. The interaction of light

with the molecule distorts the electronic cloud around the nuclei, polarizing the molecule and exciting it to a "virtual state".[51] When the electrons relax, the emitted energy provides a spectral fingerprint of the sample, which supplies information about the material's chemical composition and molecular structure.

Light and matter can interact by a materials polarizability, which is determined by the ability of the electron cloud to interact with an electric field. The incident photon can excite vibrational modes of the molecule, vibrating in a cosine pattern with a frequency proportional to the bond strength and inversely proportional to the reduced mass. As a result, each molecule has signature peaks determined by atoms in a molecule and the characteristics of their bonds.

Rayleigh scattering is an elastic scattering, where light is deflected after interacting with a molecule, but does not change wavelength. It is this process that accounts for the blue appearance of the sky, due to air molecules scattering the white light spectrum from the sun. The Rayleigh scattering of light is proportional to the fourth power of wavelength, so blue light scatters more than longer wavelengths.

The energy changes detected in vibrational spectroscopy include nuclear motion. When nuclear motion is involved there is an energy transfer occurring between incident photon to the molecule, or from molecule to scattered photon. The scattered photon can then have energy higher or lower than the incident photon. If the emitted photon has higher energy, this process is termed Stokes-Raman scattering, the latter is Anti-Stokes Raman scattering, illustrated in Figure 3.4. Anti-Stokes occurs when molecules are vibrationally excited prior to irradiation, resulting in scattered photons with frequencies above the incident frequency. Anti-stokes is rarely used, and substantially weaker than Stokes scattering.

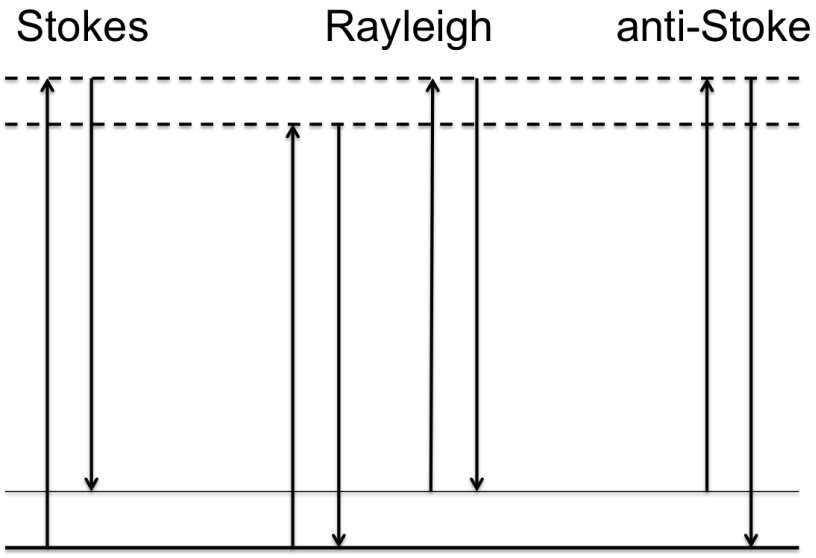

Figure 3.4: Elastic and Inelastic Raman Scatter. Stokes emission occurs as red shifted peaks, and anti-Stokes emission is blue shifted (to higher energy).

Raman spectroscopy is exceptionally better for characterization of carbon materials.[13] Carbon structures present vibrations in the Raman spectrum that are not visible in IR spectrum. In molecules that possess a center of symmetry, the rule of mutual exclusion states that normal modes cannot be both IR and Raman active.[45] Raman is highly sensitive to symmetric covalent bonds with little or no dipole moment, such as C–C bonds.[13] Raman spectroscopy is capable of detecting even slight changes in structure. The Raman band can shift, broaden or narrow, and vary in intensity. These changes can reveal the amount of stress your sample is undergoing, its crystallinity, and amount of material in the sample, respectively.[45]

Surfaced Enhanced Raman Spectroscopy (SERS)

Surfaced Enhanced Raman Spectroscopy (SERS) is a nanoscale phenomenon that occurs when molecules are adsorbed onto metallic surfaces resulting in a

significant enhancement of Raman scatter.[52] SERS arises from two mechanisms, electromagnetic enhancement and chemical enhancement.[53] The chemical mechanism is attributed to the electronic coupling between the adsorbed molecules and the surface of the nanostructured metal. The electromagnetic enhancement accounts for most of the total enhancement and manifests when a nanostructured conductor is excited with wavelengths of light from a monochromatic source that resonates with its LSPR.[52] SERS enhancement of adsorbed molecules works by amplifying the light intensity at the metals surface, increasing Raman scattering rate of the molecules.[6]

SERS has rapidly grown as a tool frequently used for recording spectra in dilute solutions, because of its high selectivity and sensitivity.[54] [32] Enhancement due to SERS can increase intensities by 10^9–10^{10}.[6] Gold nanoparticles have an LSPR band near 520nm, and are often exploited for SERS enhancement by 532nm excitation. Gold nanoparticles in particular can provide a SERS field enhancement of 10^7–10^8 on average.[6]

3.4 TRANSMISSION ELECTRON MICROSCOPE (TEM)

The smallest distance that can be resolved by the human eye is 0.1–0.2mm. Finer details can be seen by use of an optical microscope. The Rayleigh criterion, in EQ3.14, defines the resolution of a light microscope. Since the variable for refractive index and semi-angle are small in comparison to the wavelength of light (400-700nm), the resolution of an optical microscope can be approximated using just the incident light. The resolution can be approximated as half the wavelength of light. This instrument allows objects 100 times bigger, like a strand of hair, to be seen, and is great for studying other materials on the microscale (50–100 micron).

$$\delta = \frac{0.61\lambda}{\mu \sin\beta}, \tag{3.14}$$

In equation 3.14, ß is the semi-angle of collection of the magnifying lens, δ is Rayleigh criterion, λ is wavelength of incident light, and μ is refractive index.

However, smaller structures of nanoscale, like bacteria, require a high-resolution approach where electrons are used rather than photons. A transmission electron microscope (TEM) is a unique microscopy technique that passes an accelerated beam of high-energy electrons through a small area of interest. Electromagnetic coils and high voltages are used to accelerate the electrons onto the sample at high speeds. Based on wave-particle duality, electrons can behave like waves. At faster (10^7–10^8 m/s) speeds, electrons have a wavelength equivalent to about 1nm, providing higher resolution. The applied voltage determines how fast the electron travels and can be correlated to EQ3.15.

$$eV = \frac{1}{2}mv^2, \tag{3.15}$$

In equation 3.15, eV is electron voltage, m is mass, and v is velocity.

The interaction of electrons transmitted through the sample form an image that is then magnified and focused onto an imaging device.

Chapter 4

RESULTS AND DISCUSSION

The samples produced from PLAL of a gold target submerged in an ethanol bath were analyzed by various techniques. Both UV-Vis and Raman spectroscopy were utilized to determine the chemical structure of the molecules in solution. TEM was applied to investigate the structure of condensed product and crystal lattice.

4.1 UV/VIS

UV/Vis data was collected using Agilent Cary 4000 High-Performance UV/Vis Spectrometer, with a range of 175nm–900nm. Samples were placed in a micro-cuvette made of quartz. Quartz or glass cuvettes are best for UV/Vis spectroscopy, as they do not absorb light in the UV or visible range. Since ethanol is the base of every sample, it was used to generate a baseline and calibrate the UV/Vis data. The coherent motion of the free electrons in gold nanoparticles is stimulated when the spectrometer excites with a wavelength similar to the LSPR band. A large absorption peak representative of LSPR is present in the spectra between 500–600nm. The LSPR absorption peak is directly influenced by the size, shape, and composition of nanoparticles.[55] Combining UV/Vis spectra with Mie theory calculations can provide an approximation of nanoparticle size.

Mie theory calculations are difficult to execute analytically, as a result, Mie theory equations were collectively used to generate a python program capable of determining nanoparticle size from LSPR absorption peaks.[50] Python simulations were performed for gold nanoparticles up to 150nm in diameter, shown in Figure

4.1. The simulation predicted the LSPR peak would move towards longer wavelengths, eventually presenting a shoulder, as particle size increased.

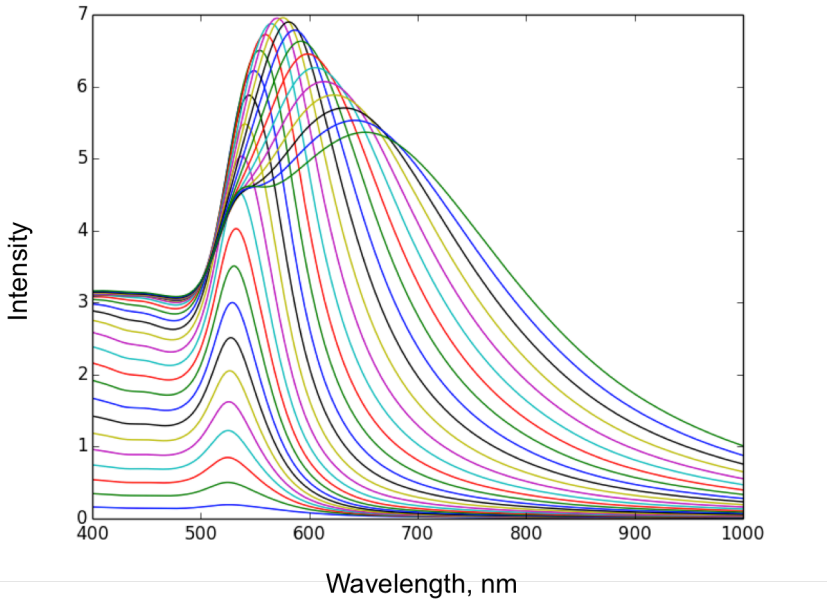

Figure 4.1: Python simulation for different nanoparticle sizes, displaying LSPR peak shifting towards the right as particle size increased.

The peak centers from the simulation were fitted and a trend line was generated shown in Figure 4.2. The trend line shows the corresponding wavelength and LSPR peaks associated with particle size. According to Figure 4.2 nanoparticles less than 40nm all present similar LSPR absorption peaks. Once diameters surpass 40nm LSPR peaks considerably move towards longer wavelengths. Due to intrinsic confinement, nanoparticles <5nm display a dampened LSPR peak and are not accurately represented by Mie theory calculations.[6]

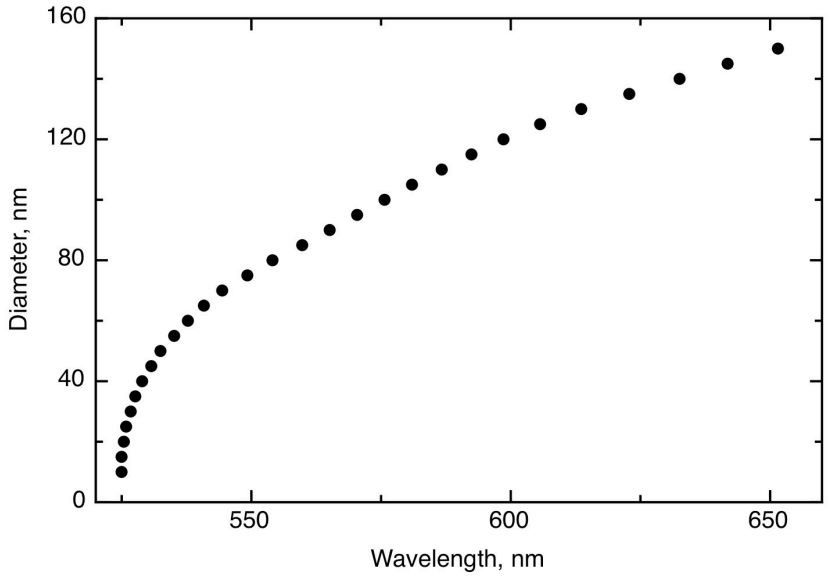

Figure 4.2: The surface plasmon absorption band shifts with the increasing diameter of gold nanoparticles. At small sizes (below 20 nm in diameter), the band is centered around 525 nm and grows to roughly 575 nm when the nanoparticles reach 100 nm according to Mie theory.

After PLAL, the final samples extracted from the beaker were no longer clear and varied in color. Gold nanoparticles have a double layer potential surrounding the sphere that repels other gold nanoparticles. This repulsion force is what keeps them in colloidal suspension throughout a solution, resulting in a uniform color. Samples generated at low-power conditions were pink or ruby red, while samples generated under high-power conditions were light to dark purple. Typically, the bright ruby red samples transitioned to a light purple color within 15-20min. UV/Vis spectroscopy was immediately performed on a bright ruby red sample and data was collected every ten minutes for a total of one hour. The spectra representative of this sample is shown in Figure 4.3, where an absorption peak shift is apparent.

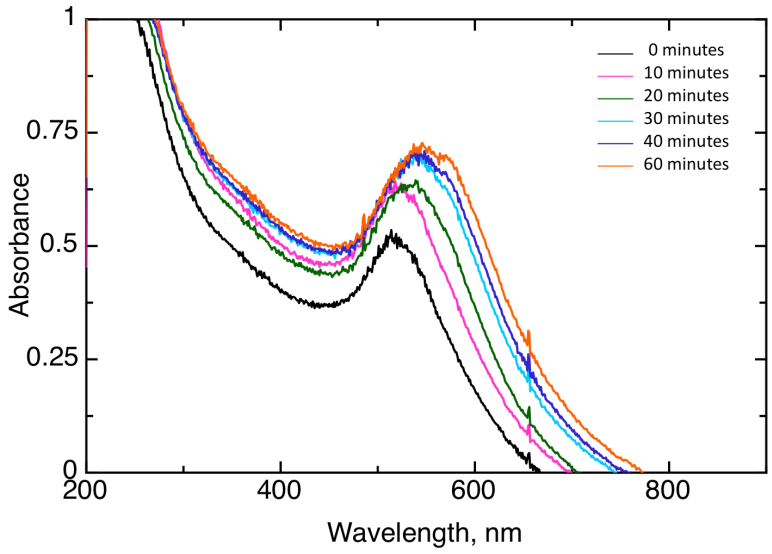

Figure 4.3: UV/Vis plot showing absorbance shift of gold nanoparticles over a period of time due to surface plasmon resonance.

The peaks from the absorption spectra were fitted using proFit software, and used in conjunction with the python Mie theory program to determine nanoparticle size.[56] Table 4.1 contains all the fitted data such as, LSPR peaks and nanoparticle diameters, taken over the one-hour time span. The fitted LSPR peak taken at 0 minutes remained the same after 10 minutes. However, after 20 minutes gold nanoparticles aggregated from being <5nm to large clusters averaging 59nm in diameter, a significant increase in size. After 30 minutes, the clusters grew larger to a size of 73nm. At the end of 60 minutes, nanoparticles began to lose potential and clusters remained under 83nm. The total LSPR peak shift went from 524nm to 557nm within an hour time. The LSPR peak intensity increases as larger clusters absorb more light passing through. The absorption peak taken at one hour also displays a small shoulder predicted by Mie theory calculations.

Table 4.1: Red shift of peaks seen in sample over a one-hour time frame

Time	Peak (nm)	σ	FWHM (nm)	Intensity	Diameter (nm)
10	524.57	30.39	71.4165	0.2	< 5
20	536.9	49.98	117.453	0.33	59
30	547.58	53.66	126.101	0.34	73
40	552.16	57.07	134.1145	0.36	78
60	557.77	60.26	141.611	0.38	83

The full width half max (FWHM) can be determined by the standard deviation, using EQ4.1 The FWHM value reflects how long the lifetime of plasmon is, where larger values depict shorter lifetimes.

$$FWHM = 2\sigma\sqrt{2ln2}, \tag{4.1}$$

In equation 4.1, σ is standard deviation.

The different LSPR absorption peaks explain the different colors seen in samples. The nanoparticles formed under low-power conditions absorb blue-green and reflect red light. The interaction of light with very small nanoparticle causes the colloidal sample to appear red. The larger clusters interact differently with light and begin to reflect blue light and yield purple samples. The visible transition of samples from ruby red to purple is described by the trend line shown in Figure 4.2. The moment nanoparticles exceed a size of 40nm, wavelengths immediately move towards the red spectrum in which a physical change in color is observed.

The bright red solutions contained small gold nanoparticles of larger concentration than the light pink. The dark purple samples contained a high concentration of larger, aggregated particles. Experiments were typically carried out under high-power conditions and were shown to form products of interest. The UV/Vis analysis identified nanoparticles of approximately 5nm were needed for

catalysis during synthesis. Once catalytic characteristics were exploited during experimentation, the nanoparticles of this size were no longer needed. After 24 hours gold nanoparticles lost their potential and settled to the bottom of the container, forming a distinct supernatant and pellet.

To expedite separation, samples underwent a purification process, which removed large gold nanoparticles and isolated carbon structures of interest. Nanoparticles of 2nm in diameter or smaller were not removed by purification and were still seen in final samples. UV/Vis spectra of purified samples did not display an LSPR absorption peak since 2nm gold nanoparticles exhibit intrinsic confinement. Purified samples revealed absorption peaks between 200-300nm. The absorption range is explained by excitation from the highest energy bonding pi-orbital (HOMO) to the lowest energy anti-bonding pi-orbital (LUMO) in the carbon molecule. Samples consistently show three peaks in the 200nm absorption spectra. The absorption spectra, shown in in Figure 4.4, presented UV/Vis peaks at 259nm, 265nm and 271 nm.

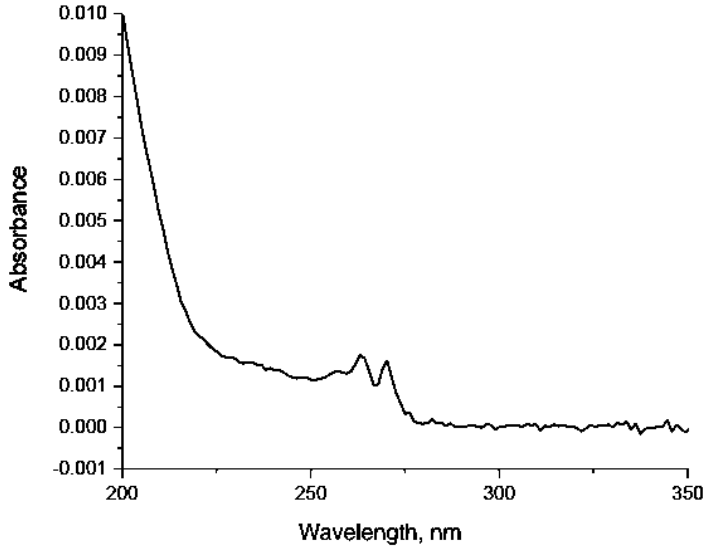

Figure 4.4: UV/Vis plot of pseudocarbyne sample showing π→π* bonding peaks of interest. Three peaks are observed. Peaks are observed at 259, 265, and 271,with a FWHM= 7.36, 4.14, 3.68 nm, respectively.

The variation in peaks could result from the formation of carbon rings and carbon chains. The peak shift could be directly correlated to the amount of strain carbon chains endure. Literature describes a similar circumstance when comparing the amount of strain imposed on tetrynes.[26]

4.2 RAMAN

The vibrational properties of synthesized carbon samples were measured by Raman spectroscopy. The specific carbon hybridization of synthesized sample can be determined by comparing Raman peaks to literature values. Sample excitation was performed with an ONDAX 633nm laser diode. A red, 633nm light was used over 532nm or other wavelengths, to maintain low fluorescence, achieve more surface penetration, and prevent sample damage.[57] The output signal was sent to the InSpectrum 300, Acton Inc. spectrometer. Raman analysis was performed on raw

and purified samples to determine if signature peaks were present in both. Wet and dry samples were also utilized to understand whether the carbon molecule required a liquid environment for stability. Power was maintained under 10mW for sample excitation, use of higher power created burn spots in the sample and caused many peaks to vanish.

Samples were deposited onto glass microscope slides. Glass slides with a concave center were used to contain wet samples in a localized spot. A thin glass square was placed overtop to prevent the ethanol from evaporating. The glass slide was fixed under the (Mitutoyo: FWHM = 1 x 1.45μm) microscope with 50X objective. The combination of 633nm light, 50X objective, and an output power of 5–10mW, produced considerable background signal, and Raman data was unable to be collected due to the interfering fluorescence of the glass. To prevent major fluorescence, aluminum was replaced as the substrate. A small cavity was molded with aluminum for wet samples. The aluminum substrate reduced fluorescence, however, it did not eliminate it completely. A precise focus on the sample is crucial when performing Raman on small concentration of sample. The rigid surface of the aluminum made it very difficult to acquire an exact focus and hindered progress. The aluminum was replaced with several substrates throughout the course of these experiments. As, a result, use of glass, aluminum, and germanium substrates will be seen in the Raman data. The collected spectra were calibrated using cyclohexane as the control. Cyclohexane provides large, distinct peaks that are easily attainable without the need of a precise focus. Characteristic Raman peaks for cyclohexane are observed at 803cm^{-1}, 1029cm^{-1}, 1267cm^{-1}, 1446cm^{-1}, 2853cm^{-1}, 2886cm^{-1}, 2923cm^{-1}, and 2838cm^{-1}. The laser was set to max power of 74mW and collected for one second and one accumulation. The experimental cyclohexane peaks were cross-referenced

with literature values for cyclohexane to generate a linear equation. The Raman peaks collected for samples were fitted into the equation to calibrate data.

Since pseudocarbyne synthesis is carried out in liquid ethanol, Raman data of wet samples can contain ethanol peaks. A Raman spectrum of ethanol was taken to determine if peaks present are associated to ethanol or other constituents. Signature Raman peaks for Ethanol (C_2H_5OH) are shown in Figure 4.5 below. The most prominent peak at 882cm^{-1} is representative of C–C stretching. The two peaks at 1050cm^{-1} and 1092cm^{-1} exhibit C–O stretching and CH_3 rocking, respectively. While the 1447 cm^{-1} peak is a result of CH_3 bending. More ethanol peaks are located higher in the Raman spectrum between 2800cm^{-1}–3000cm^{-1} and are representative of C–H stretching.

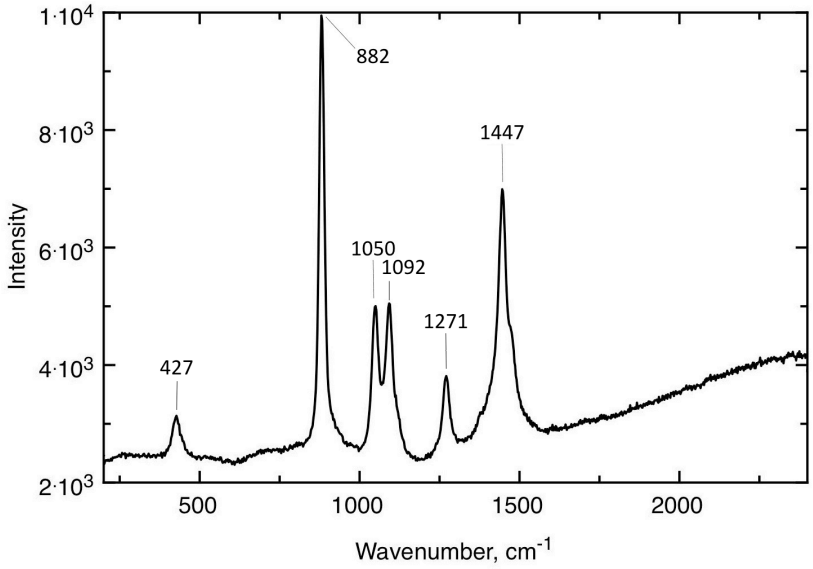

Figure 4.5: Raman spectra of ethanol. Signature peaks are observed at 427, 882, 1050, 1092, 1271, and 1447 wavenumbers. These peaks are assigned to vibrational motions in ethanol as described in the text.

The inclusion of gold during synthesis led to the assumption samples would exhibit SERS, a 10^{10} enhancement of Raman spectra. Since gold nanoparticles have

an LSPR band close to 530nm, a 532nm laser would excite electrons to real electronic states rather than virtual.[58] However, no SERS was observed with 532nm excitation. The absence of SERS was due to the aggregation of gold nanoparticles, which generated local hotspots, resulting in a red shift of the LSPR band.[58] Samples were excited with 633nm light in attempts to exploit the SERS phenomenon. According to UV/Vis data, the colloidal gold found in raw samples is approximately 12nm in diameter, while the purified samples contain gold nanoparticles approximately 2nm in diameter. Purified samples are stripped of colloidal gold and only contain small (<2nm) gold nanoparticles. When gold nanoparticles reach a diameter of 3nm or smaller, they no longer exhibit SERS.

Samples were generated under high and low power conditions to confirm whether an ablation threshold existed for generating sp^1 carbon. Samples of low power had a laser intensity of 0.05–0.2 GW/cm^2, while high power experiments had an intensity of 0.625–0.7 GW/cm^2. The spectrum shown in Figure 4.6 was taken from a sample produced under low power conditions. The sample was dried on an aluminum substrate and excited with 4.5mW of 633nm light. The sample produced broad peaks at 1577cm^{-1} and 2874cm^{-1}, known to be G and G' peaks, respectively. The G band is the first-order Raman band and G' is second order Raman band of all sp2 hybridized carbon materials.[59] A more intense G' peak suggests graphene is present in the sample.[59] Other carbon structures may be present in low concentrations, however sp^2 sites primarily dominate the Raman spectra of carbon films, due to vibrational excitation resonating with the π states.[60] Additional low-power samples produced similar Raman spectra, also lacking peaks representative of sp^1 carbon.

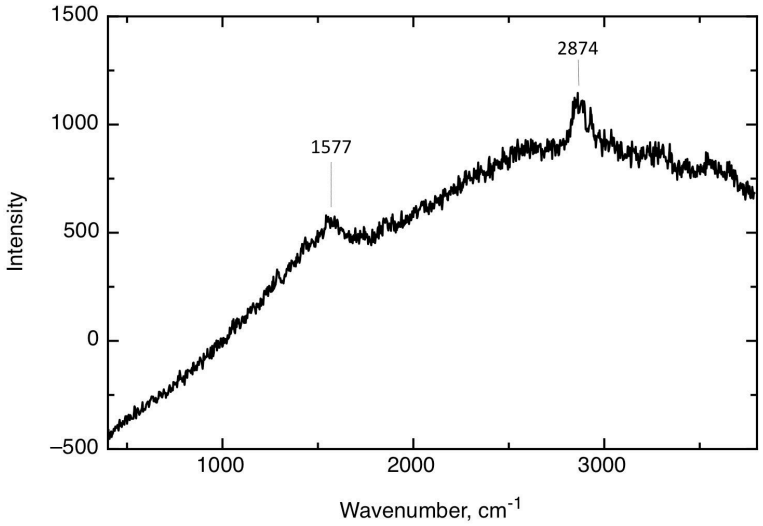

Figure 4.6: Low power ablation of gold in ethanol produces sp^2 carbon Raman signatures. Broad peaks at 1577 and 2874 cm^{-1} are assigned to sp^2 carbon. A broad fluorescence peak centered at ~3000 cm^{-1} is attributed to the aluminum foil substrate.

High-power samples were generated under the theoretical ablation threshold. Samples were predicted to contain carbon molecules, acetylenic in structure with alternating single and triple bonds. The Raman spectrum for high-power sample is shown below in Figure 4.7. The sample was centrifuged then deposited onto a small germanium plate until it dried. This process was repeated in order to concentrate the sample. An output power of 1.0mW was used to excite the sample. Applying a power of 4.5mW or more created burns spots in the sample. The germanium peak is seen at 289cm^{-1}. The peak at 407cm^{-1} is unidentified. The broad peak at 1529cm^{-1} is the G band for sp^2 carbon. When an excitation power of 4.5mW was used, the peak at 998cm^{-1} disappeared and the broad 1529cm^{-1} peak expanded, forming three separate peaks. The three peaks were 1287cm^{-1}, 1346cm^{-1}, and 1550cm^{-1}. Literature suggests 1287cm^{-1} is sp^1 C_2H_2, while 1346cm^{-1} and 1550cm^{-1} are the G and D bands for amorphous sp^2 carbon, respectively [61,62]. The peak at 998cm^{-1} is close to the 991cm^{-1} peak for alpha ring stretching of benzene. This may suggest carbon rings

are present in the sample and are sensitive to laser power. The final peak at 2125cm^{-1} is located in the 2100cm^{-1} region, attributed to sp^1 carbon. Comparing this peak with established carbon molecules shows a similarity with 1-Hexyne (C_6H_{10}). The carbon structure, 1-Hexyne has a very prominent peak at 2120cm^{-1}; however, nine additional peaks also exist for this molecule that are not present in the Raman spectra. The comparison to 1-Hexyne suggests an entirely different carbon molecule is present in the sample.

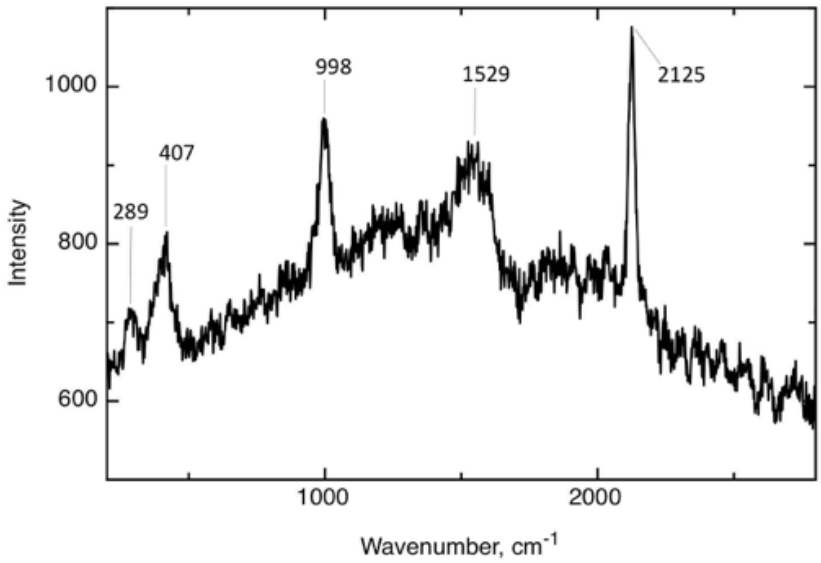

Figure 4.7: Raman spectra of an unpurified sample prepared under high laser power on a germanium substrate. Raman peaks are observed as described in the text.

The Raman spectrum for a centrifuged, high-power sample is shown in Figure 4.8. Raman was performed on a wet sample, rather than dry to determine whether the stability of certain structures was dependent on the liquid environment. The peak located at 289cm^{-1} is representative of the germanium substrate, and the following peak at 735cm^{-1} is attributed to sp^2 amorphous carbon.[63] Again, the 969cm^{-1} peak could be representative of carbon rings, similar to the previous 998cm^{-1} peak.

All unlabeled peaks are attributed to ethanol, and are expected to appear in a wet sample. At the far (right) end of the spectrum four peaks are seen, with two peaks present in the 2100cm^{-1} region. The furthest peak located at 2232cm^{-1}shows similarity to 4-Octyne (C_8H_{14}) with a peak at 2239cm^{-1} and with 2-Heptyne (C_2H_{12}) with a peak at 2235cm^{-1}. However, both known carbon structures are accompanied by additional peaks primarily around 3000cm^{-1} in their spectra due to C-H stretching, and more between 1300cm^{-1} and 1450cm^{-1}.

The next two peaks are at 2149cm^{-1} and 2100cm^{-1}. Typically peaks at 2100 cm^{-1} suggest sp^1 carbon. The first peak is at 2073cm^{-1} and shares close resemblance to the 2175cm^{-1} for Octatetrayne (C_8H_2), as well as, 2070cm^{-1} for Hexayne ($C_{12}H_2$). [61,64]

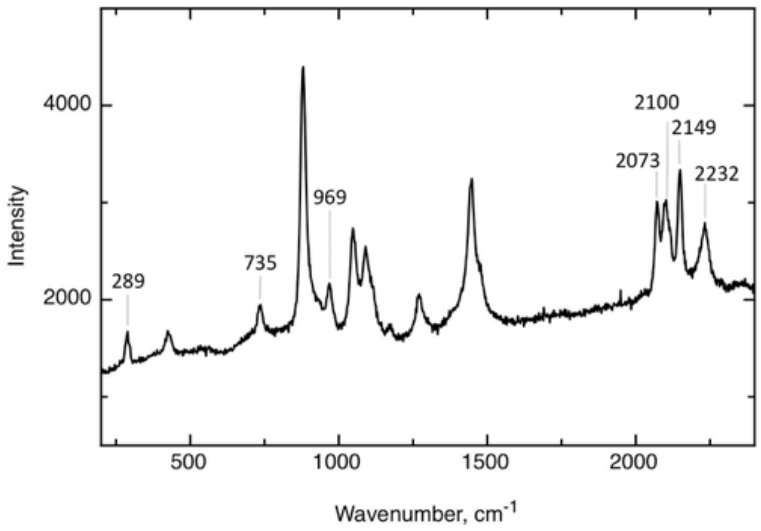

Figure 4.8: Raman spectrum of a wet sample. Unlabeled peaks are assigned to ethanol as described and shown in Figure 4.5. The peak at 289cm^{-1} is assigned to the germanium substrate, and the rest are materials produced through the laser ablation experiment.

DFT calculations, shown in Figure 4.9, were generated to predict Raman spectra for different sp^1 carbon molecules. The acetylenic, gold stabilized structures,

1,3,5,7,9-Decapentayne ($Au_{12}C_{10}H_2$) and 1,3,5,7,9,11-Dodecahexayne ($Au_{12}C_{12}H_2$), were calculated to have signature peaks between 2100cm^{-1}-2170cm^{-1}.[29] The variation in peak location is highly influenced by the carbon chain length. The adsorbed gold particles are on the subnanoscale, approximately 0.3nm in diameter. The addition of gold nanoparticles and clusters to the carbon chain can result in kinks. The peaks at 2232cm^{-1} and 2100cm^{-1} in the previous spectra, shown in Figure 4.8, were cross-referenced with DFT calculations and showed to align well with computations for $Au_{12}C_{12}H_2$. Similarly, the peak at 2149 cm^{-1} aligned well with calculations for $Au_{12}C_{10}H_2$. The slightly larger wavenumber is due to a shorter carbon chain.

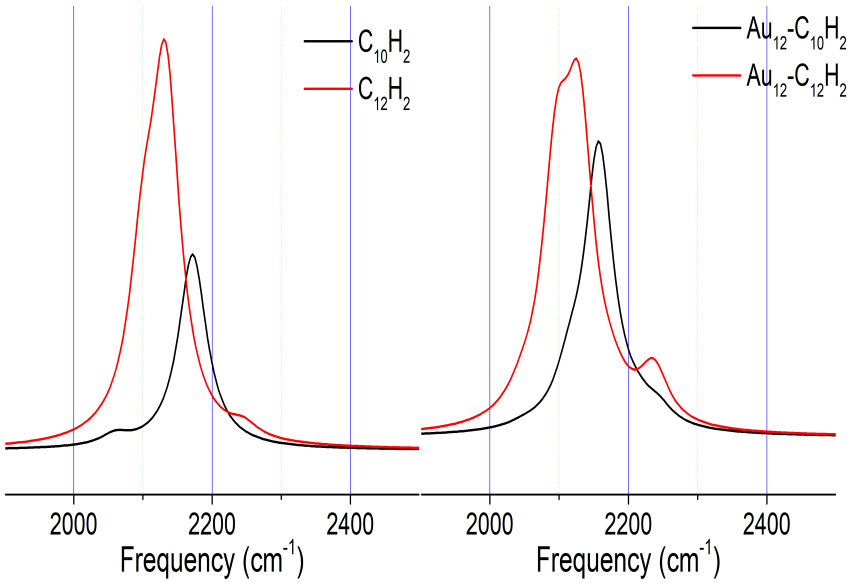

Figure 4.9: DFT calculations demonstrate the signature peaks when gold clusters are bound to linear carbon-chain molecules. Reprinted from [29]

To isolate desired components and remove the presence of sp^2 carbon, high-power samples were purified before conducting Raman spectroscopy. The solution was dried and concentrated on an aluminum substrate and excited with 10mW of 633nm light. Purification of sample is necessary because sp^2 vibrations dominate

Raman spectra. If sp^2 carbon is present, other peaks may be diminished. Samples must contain a significant concentration of sp^1 carbon to see intense Raman peaks.[60] The spectra produced two separate peaks in two different areas of the sample. The first peak, in Figure 4.10, was located at 2135cm^{-1}, representative of carbon triple bonds.[61] Specifically, 2135cm^{-1} can be attributed to the carbon triple bonds of $Au_{12}C_{12}H_2$.

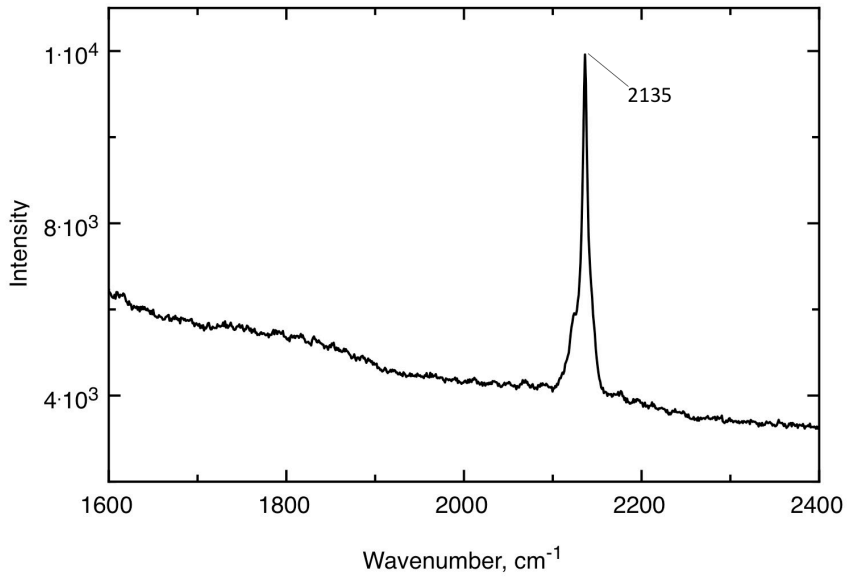

Figure 4.10: Raman spectrum of a purified sample that is prepared under high laser power. The peak at 2135 cm^{-1} matches theoretical predictions for to $Au_{12}C_{12}H_2$.

The spectra also displayed a peak at 2177cm^{-1}, shown in Figure 4.11. A peak at 2177cm^{-1} is representative of sp^1 carbon triple bonds. Referencing DFT calculations, the peak can be correlated to the carbon triple bonds of $Au_{12}C_{10}H_2$. While both peaks were seen throughout the same sample, they typically were not seen in the same location. Both peaks are of great intensity, suggesting a large concentration of product is present. Additionally, the thin, narrow peaks with FWHM of 18.8cm^{-1} and 3.99cm^{-1} represent crystalline structures.

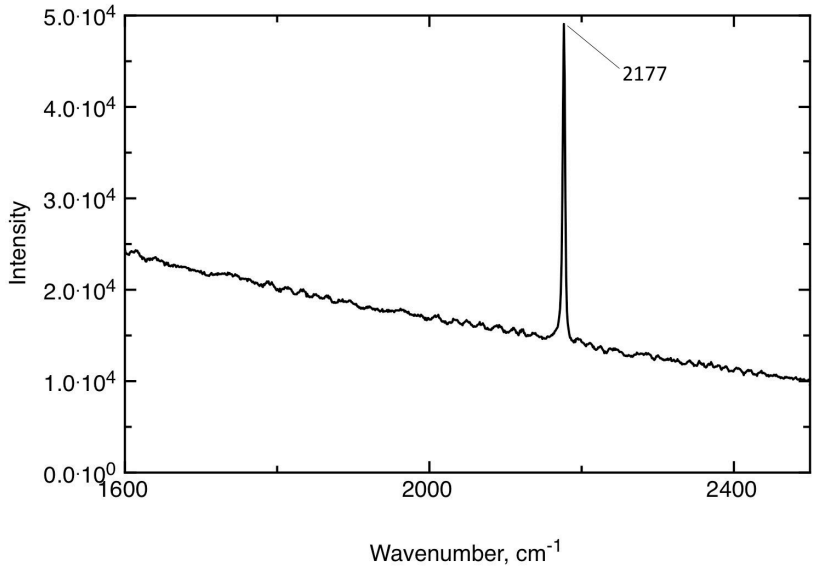

Figure 4.11: Raman spectrum of a purified sample that is prepared under high laser power. The skinny peak at 2177 cm^{-1} is assigned to $C_{10}H_2$.

The spectrum in Figure 4.12 comes from a sample produced under high-power conditions and excited with 4.5mW of 633nm light. The only peak that was seen was at 522cm^{-1}. Literature states peaks in this low frequency are attributed to the bending of sp^1 carbon chains. [63] DFT calculations for $Au_{12}C_{10}H_2$ produce a peak in the 500cm^{-1} region. This peak was cross-referenced with a carbon database, and showed peak similarity to Naphthalene ($C_{10}H_8$), which has a small peak at 514cm^{-1}. While, both carbon structures are composed of ten carbon atoms with variance in hydrogen atoms and gold adsorption, Naphthalene incorporates nine additional peaks with a prominent one at 1382cm^{-1}.

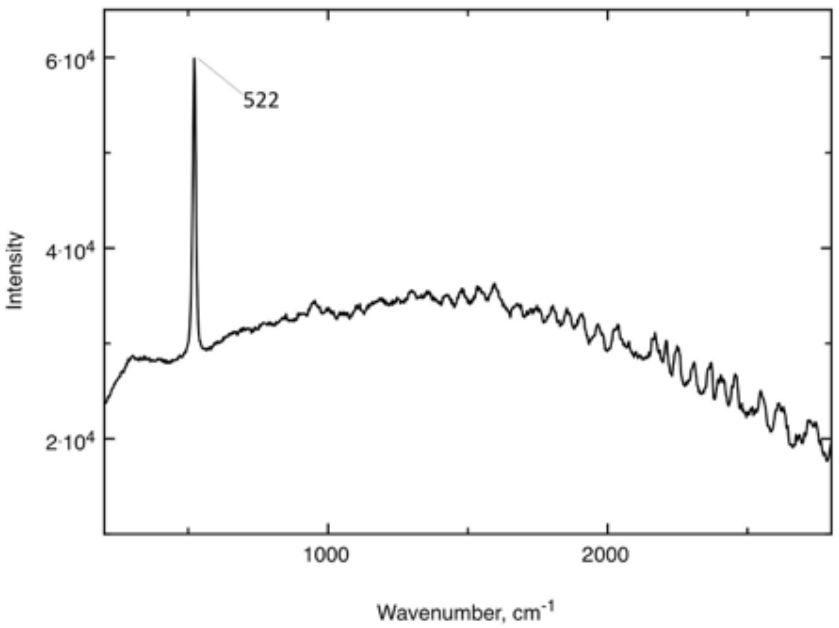

Figure 4.12: Raman spectrum of a purified sample that is prepared under high laser power. The peak at 522 cm^{-1} is attributed to sp^1 C–C single bond stretching.

The final spectrum is shown in Figure 4.13, which comes from a purified, high-power sample. The most prominent Raman peaks are located at 980cm^{-1} and 2071cm^{-1}. The 980cm^{-1} can be correlated to C–C single bond stretching. A peak at 2071cm^{-1} was seen in previous spectra and is representative of singlet and triplet C_{12} carbon structure.[29] The peaks at 1058cm^{-1} and 1120cm^{-1} can also be correlated to C–C single bond stretching. While, the peak at 1120cm^{-1} matches well with DFT calculations for C–C single bond stretching in $Au_{12}C_{12}H_2$.

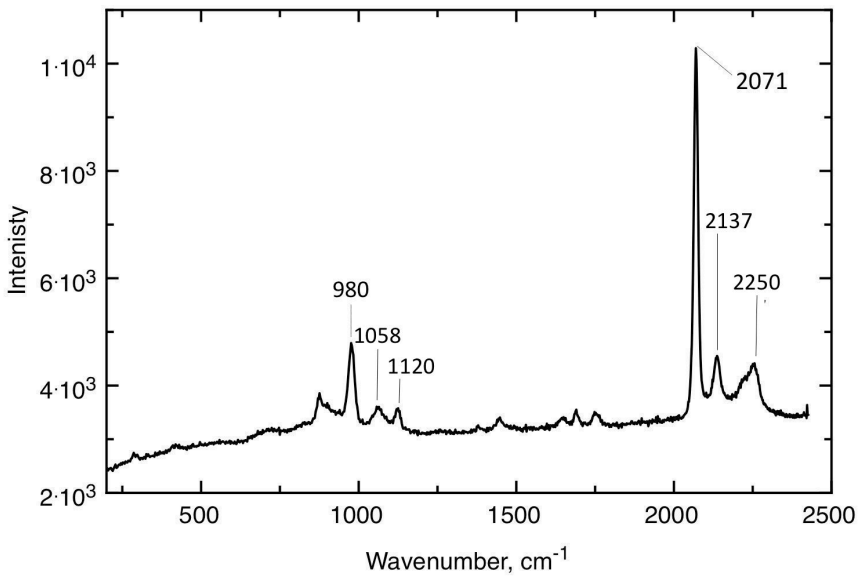

Figure 4.13: Raman spectrum of a purified sample that is prepared under high laser power.

4.3 TEM

TEM analysis was performed using a Philips CM200-FEG high resolution TEM and JEOL JEM 2010F for scanning transmission electron microscopy (STEM). These techniques were used to help visualize the nanoscale structure, crystalline or amorphous features, and determine grain boundaries of product. TEM/STEM was performed on both raw and purified samples. For preparation, a wet sample was dropped onto lacey carbon coated type-A300 mesh copper grids. All TEM images were analyzed using ImageJ software.[65]

Raw samples contained a combination of small (<5nm), gold carbon structures, and large (>5nm) gold nanoparticles in colloidal suspension. The colloidal gold nanoparticles aggregated over a period of time, forming large networks. Figure 4.14 shows these large networks of aggregated particles, present throughout the grid.

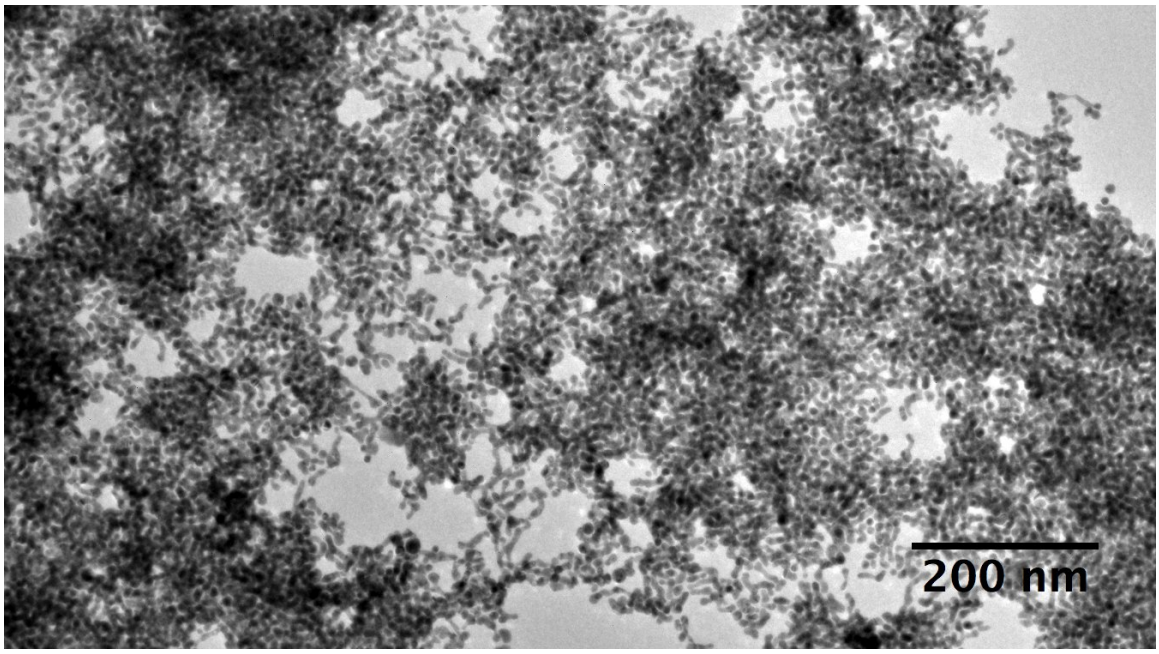

Figure 4.14: a) TEM image of a raw (unpurified sample) laser ablation of gold material. The size distribution of the gold nanoparticles is uniformly distributed around 10–15 nm in diameter. Some indications of lines of nanoparticles are observed.

During synthesis, a 532nm laser can reirradiate gold nanoparticles and selectively heat them until they reach melting points. As a result, several areas contain fused gold nanoparticles, shown in Figure 4.15-a, that form elongated chains. The lattice spacing of the gold nanoparticles are visible upon further magnification, shown in Figure 4.15-b, where the superimposed fringes are shown crisscrossing.

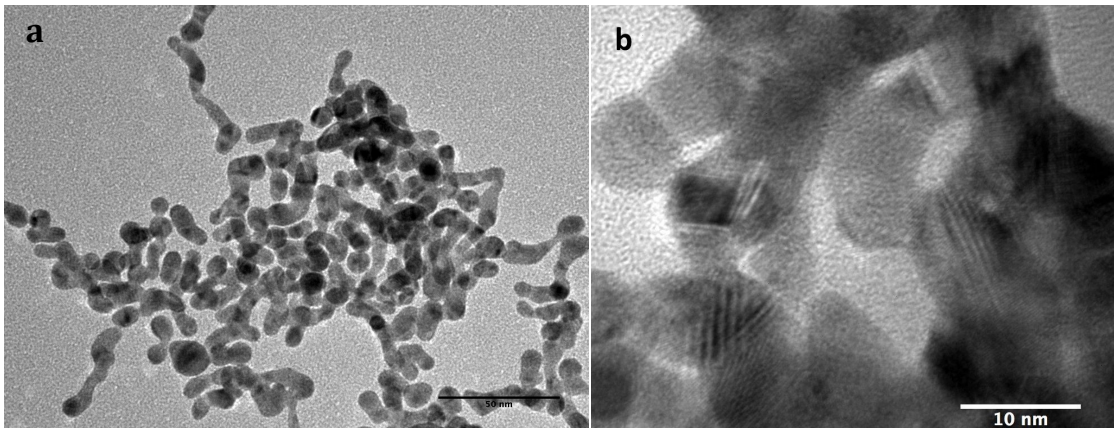

Figure 4.15: a) TEM image of fused spherical gold nanoparticles are prepared from long ablation, form elongated chains b) image represents gold nanoparticles with "crisscrossed" fringe spacing.

A selected area electron diffraction (SAED) pattern, shown in Figure 4.16 below, is from an individual gold nanoparticle and was obtained by the Fourier transform of a TEM image. The d-spacing for (111), (002), and (022) planes of face-centered cubic gold (FCC) were measured and compared to literature values. The ring pattern in the SAED image produced a (111) fringe spacing of 0.235nm, (002) spacing of 0.024nm, and a (022) spacing of 0.140nm, which confirm a polycrystalline gold. Four distinct radii are expected in the pattern, but only the first three are assigned. According to Table A1, the fourth ring should appear at 0.12nm, but was not observed. The angular distribution of the bright spots indicates the orientation of the lattice with respect to the image. A continuous ring would indicate multiple crystals oriented in all directions. An amorphous crystal would not contain these patterns. If the area selected by the aperture of the TEM to obtain an SAED pattern contains only a few crystals the diffraction pattern is composed of bright spots aligned along a defined radial distance but are not continuous rings. If the number

of crystals selected in the TEM is large and oriented randomly, the diffraction pattern may provide continuous rings.

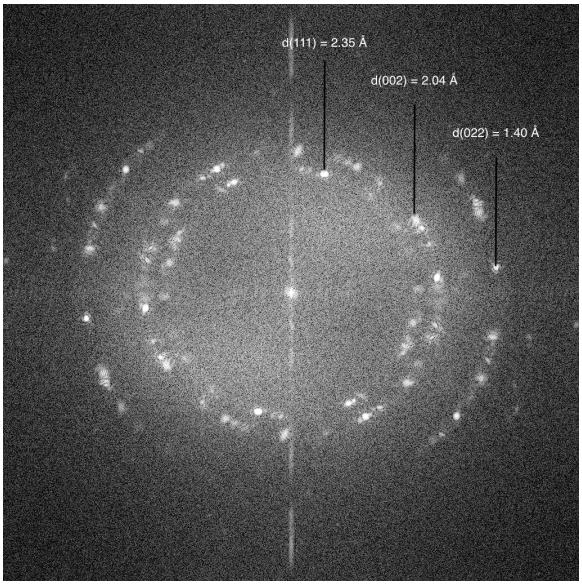

Figure 4.16: Selected Area Diffraction pattern of gold nanoparticles. The radii of the rings are related to the diffraction pattern of the lattice of gold. The d-spacings can be assigned to gold. The angular distribution of the bright spots means nothing.

The overpopulated gold nanoparticle networks made it difficult to see any product of interest. To prevent gold nanoparticle obstruction, raw samples were purified. At first glance, purified samples showed a distribution of amorphous grains 300–400nm in size, attached to the grid walls. Figure 4.17 shows a singular 360nm amorphous grain attached to the substrate. The amorphous grain is composed of small gold nanoparticles around 2nm in diameter. The gold nanoparticles embedded in the sample, do not surpass a diameter of 4nm.

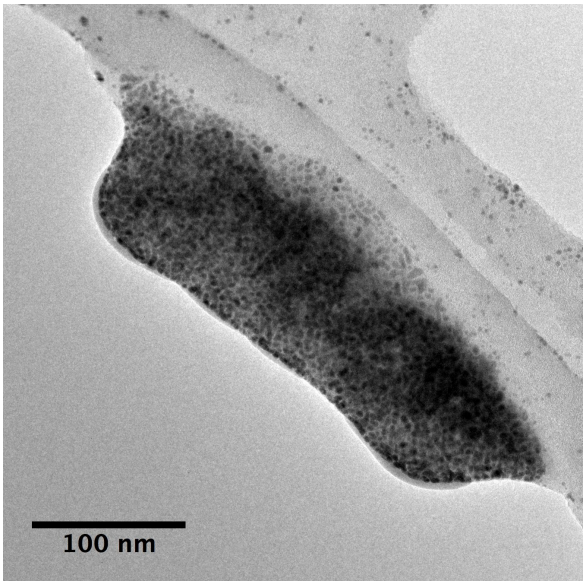

Figure 4.17: A 300 nm grain of material containing of gold clusters as observed with TEM. Similar grains are observed throughout the sample and attached to the grid.

Magnifying onto the grain revealed many streaks, representing amorphous fringes shown in Figure 4.18-a and b. The disordered fringes were parallel to one another and appeared in conjunction with gold nanoparticles. These amorphous fringes were sensitive to beam exposure and faded away after prolonged exposure.

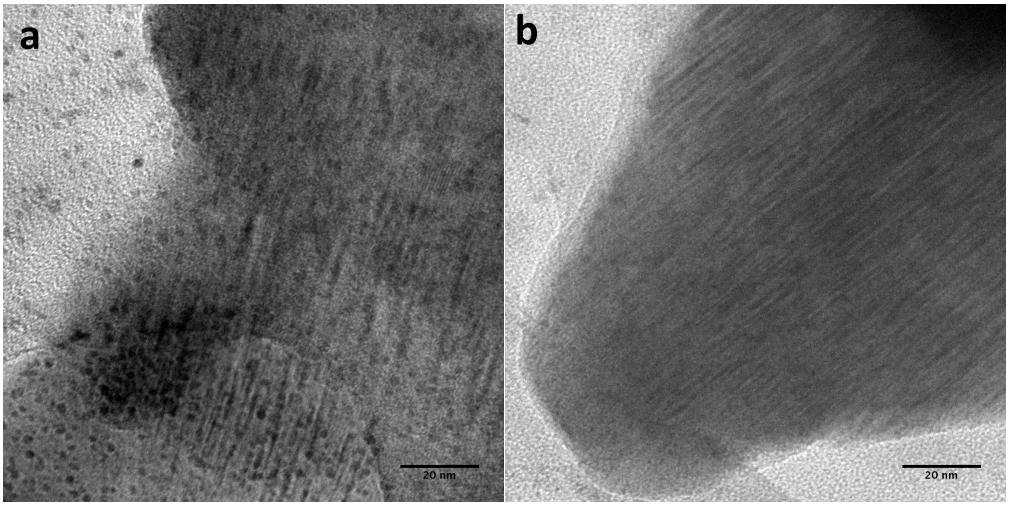

Figure 4.18: Amorphous fringes seen throughout the grain a) with gold nanoparticles present and b) without any visible particles present.

A scan throughout the whole grain further revealed large lattice fringes, shown in Figure 4.19-a and b, alongside gold nanoparticles about 1nm in diameter. Both amorphous and ordered fringes were seen patched side-by-side, throughout the large grain.

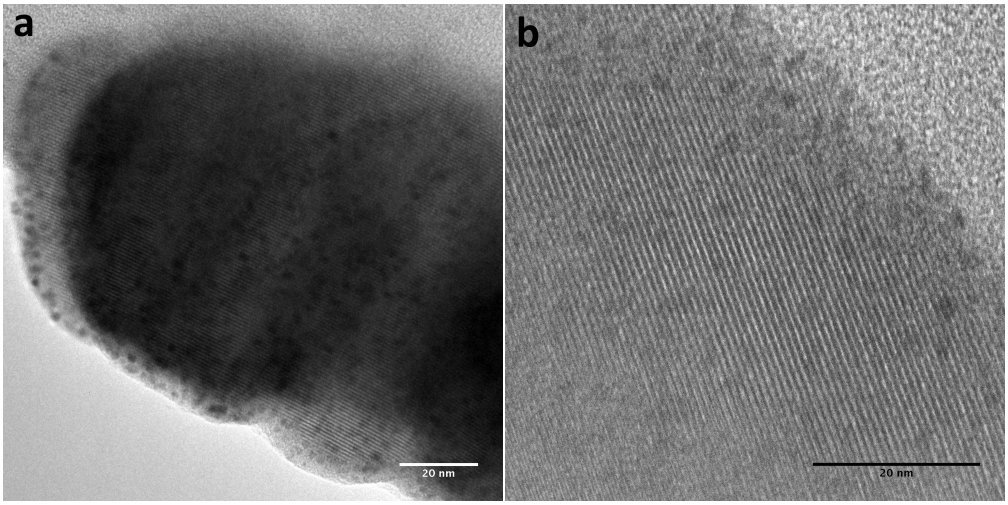

Figure 4.19: Ordered sample fringe spacing's of 0.86 nm are observed where dark spots are assigned to gold clusters of roughly 1 nm in diameter. a) TEM image with a thick sample in the center and a thin layer at the boundary (b) magnified TEM image of fringes

A Fast Fourier Transform (FFT) of the sample, shown in Figure 4.20, helped determine the spacing of the lattice fringes. The SAED technique was applied to the fringes observed for the new material to measure the lattice spacing. The new material had fringe spacing's measured to be 8.55 Å.

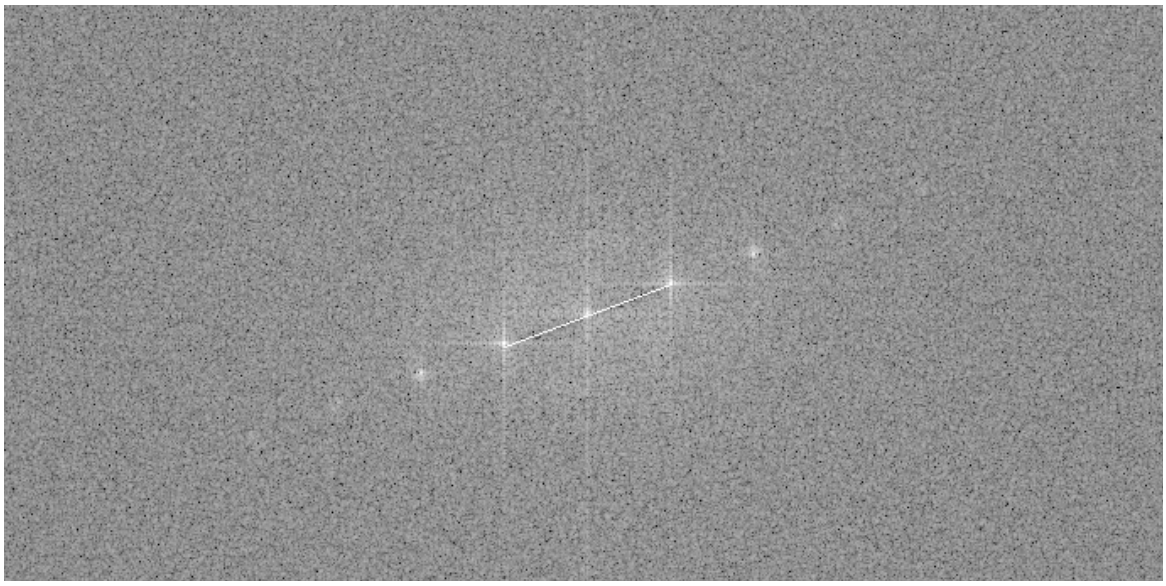

Figure 4.20: SAED pattern of new material, where fringe spacing was measured to be 8.55 Å.

The lattice spacing was cross-referenced with various carbon structures. Common carbon allotropes, such as diamond and graphite, have lattice spacing's of 3.56Å and 2.46Å, respectively.[60] A carbon mineral known as Kratochvilite, $(C_6H_4)_2CH_2$ has orthorhombic unit cell parameters a = 8.365Å, b = 18.745Å, and c = 5.654Å, found in Table A2. The spacing for Kratochvilite of 8.365Å is the closest to that of the carbon sample. However, when the sample was rotated by 30° in 5° increments to locate any overlapping fringes, no additional fringes were revealed.

The sample showed sensitivity to the high electron dose of beam within seconds of exposure. The over exposure led to a thickening around the edges of the grain and darkening and growing of the nanoparticles. The thickening growth around the edge of the grain was observed to have a crystalline structure, and was measured by the SAED technique, resulting in a fringe spacing of 5.6Å. Figure 4.21-a shows these fringes are at a 176° angle and are not aligned with the 110° angled fringes of the carbon chains. This indicates the growth is a new layer of material

that is being deposited with the application of the electron beam and therefore is termed beam damage. The growth and crystallinity due to beam damage suggests the formation and contamination of hydrocarbons. Beam exposure also led to the enlargement of gold nanoparticles. Gold nanoparticles enlarged from 2–3nm up to 6–10nm due to beam exposure, shown in Figure 4.21-b.

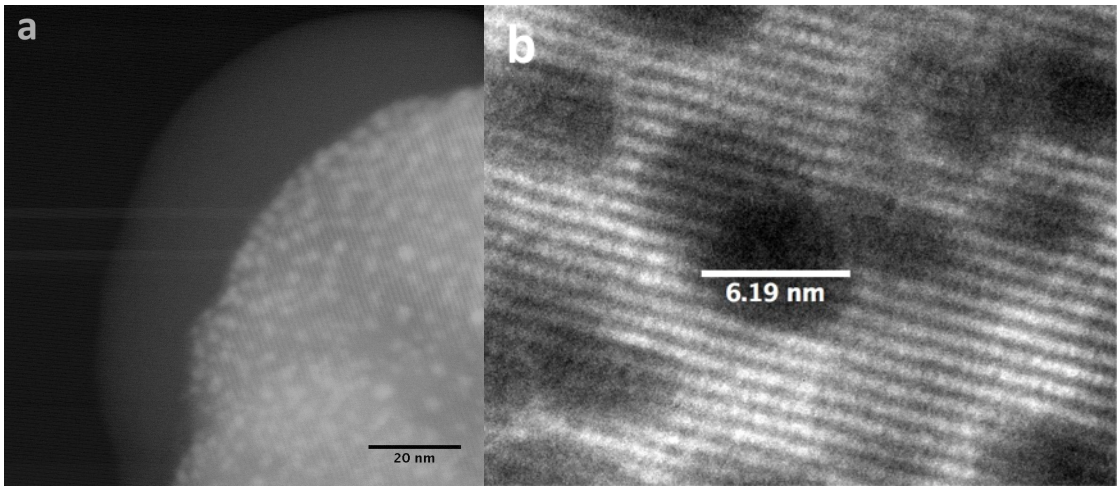

Figure 4.21: a) electron beam damage shows a crystalline form that is not aligned (new material shows lattice direction of 176 degrees) with the sample material (lattice angle of 110 degrees in this image. b) the gold clusters exhibit a continuous growth with the electron beam. The particles show a growth from ~2 nm to 6.19 nm before the beam was turned off.

4.4 DISCUSSION

Acetylenic carbon chain synthesis was carried out by the PLAL method. UV/Vis and Mie theory calculations determined gold nanoparticles of 5nm in diameter were needed for catalysis during synthesis. Purified samples displayed three peaks in the absorption spectra between 200-300nm, characteristic of sp^1 carbon.

Raman peaks from samples produced under low-power conditions only displayed signature peaks for sp^2 carbon. Low power conditions fell below threshold

range and were unable to supply the system with temperature requirements for sp^1 carbon synthesis. On the other hand, high power conditions provided many Raman peaks attributed to sp^1 carbon single and triple bonds. Table 4.2 below shows Raman peaks of interest from samples produced under high power conditions, seen in both raw and purified samples. The 522cm^{-1} peak is attributed to the sp^1 C–C single bond stretching of a C_{10} structure. Raman peaks between 970–995cm^{-1} are generally representative of carbon rings. According to literature values, peaks at 1050–1120cm^{-1} are attributed to sp^1 C–C singlet and triplet states of C_{12}. A peak seen at 1287cm^{-1} is very close to 1288.6cm^{-1} for C_2H_2, implying other forms of carbon structures may have also formed as bi-product during synthesis. Peaks at 2073–2075cm^{-1} were frequently seen, with similarity to $C_{12}H_2$, signifying carbon chains of 12 carbon atoms are generated. Typically, Raman peaks seen in the 2100cm^{-1} range can be attributed to $Au_{12}C_{12}H_2$ and $Au_{12}C_{10}H_2$. The two peaks at 2135cm^{-1} and 2137cm^{-1} were commonly seen with great intensity in samples. These peaks can be attributed to the sp^1 C–C triple bond stretching of molecules and can be correlated to the $Au_{12}C_{12}H_2$ structure. Similarly, the 2177cm^{-1} peak appeared as a singular peak of large intensity and can be attributed to $Au_{12}C_{10}H_2$. Samples displayed some Raman peaks similar to known carbon molecules. However, additional peaks corresponding to these known carbon structures were not seen in samples.

Table 4.2: Raman peaks of interest from synthesized material

Peaks (cm^{-1})	FWHM (cm^{-1})	Description
522	13.87	$C_{10}H_8$ @ 514cm^{-1} sp^1 C–C single bond stretching
969	16.00	Carbon Rings Gold adsorption enhances sp^1 C–C single bond stretching
980	21.83	Carbon Rings Gold adsorption enhances sp^1 C–C single bond stretching
998	49.79	Carbon Rings Gold adsorption enhances sp^1 C–C single bond stretching
1058	31.73	sp^1 C–C single bonds stretching
1120	15.93	sp^1 C–C single bonds stretching of $Au_{12}C_{10}H_2$
1287	22.77	C_2H_2 @1288.6cm^{-1}
2071	25.31	$C_{12}H_2$ @2070cm^{-1}
2073	15.69	$C_{12}H_2$ @2070cm^{-1}
2100	29.98	$Au_{12}C_{12}H_2$
2125	27.97	C_6H_{10} @ $Au_{12}C_{12}H_2$
2135	23.10	sp^1 C–C triple bonds $Au_{12}C_{12}H_2$
2137	11.94	sp^1 C–C triple bonds $Au_{12}C_{12}H_2$
2149	15.98	$Au_{12}C_{12}H_2$
2177	3.99	C_8H_2 @2175cm^{-1} sp^1 C–C triple bonds $Au_{12}C_{12}H_2$
2232	30.92	$Au_{12}C_{12}H_2$

Based on TEM results, the new synthesized material contains two distinct fringes, ordered and unordered. The lattice spacing of the ordered fringes is 8.55Å. Cross-referencing this spacing with other existing carbon molecules did not provide a correlation to one specific structure. The new synthesized material only has one, singular lattice spacing. All spectroscopic techniques lead to the conclusion of completely new material.

Chapter 5

CONCLUSION AND FUTURE OUTLOOK

5.1 CONCLUSION

New products have been produced under the extreme conditions of pulsed laser ablation in liquid. The spectroscopic characterization suggests a stable sp^1 hybridized carbon structure exists and was produced from ethanol and gold. The extreme and localized conditions obtained by the PLAL technique may give rise to an entirely new class of materials.

The results presented in this thesis suggest that new acetlyenic carbon structures bound to gold clusters can be prepared using PLAL. Results were compared with existing carbon structures to determine if new material was synthesized. No other identified carbon structure displays the exclusive, singular lattice spacing as pseudocarbyne.

. These molecules have new spectroscopic signatures that have been assigned by Raman spectroscopy and yield crystalline materials that have been imaged by TEM. Future work is needed to improve the product yield and to determine mechanistic information for product formation. This entirely new class of molecules and materials may have incredible properties that approach those that are predicted for carbyne. With macroscopic qualities of materials, the chemical reactivity can be explored. It is not yet clear if these molecules can be produced with techniques other than PLAL.

REFERENCES

1. Sheng, X.-L., Yan, Q.-B., Ye, F., Zheng, Q.-R. & Su, G. T-Carbon: A Novel Carbon Allotrope. *Phys. Rev. Lett.* **106,** 155703 (2011).

2. W., V. G. The Voice of OECD Business. (2008).

3. Technology, T. U. of. Techniques for synthesis of nanomaterials (I). Available at: https://www.ttu.ee/public/m/Mehaanikateaduskond/Instituudid/Materjalitehnika_instituut/MTX9100/Lecture11_Synthesis.pdf. (Accessed: 21st March 2018)

4. Moore, G. E. Cramming More Components onto Integrated Circuits. *Electronics* 114–117 (1965).

5. Willets, K. A. & Duyne, R. P. Van. Localized Surface Plasmon Resonance Spectroscopy and Sensing. *Annu. Rev. Phys. Chem.* **58,** 267–297 (2007).

6. Langer, J., Novikov, S. M. & Liz-Marzán, L. M. Surface plasmon resonance in gold nanoparticles: a review When plasmonics meets membrane technology A Politano, A Cupolillo, G Di Profio et al. - Sensing using plasmonic nanostructures and nanoparticles. *J. Phys. Condens. Matter* **29,** (2017).

7. Buzea, C., Pacheco, I. I. & Robbie, K. Nanomaterials and nanoparticles: Sources and toxicity. *J. Vac. Sci. Technol. A Vacuum, Surfaces, Film. J. Vac. Sci. Technol. A Vacuum, Surfaces, Film. Chinese J. Chem. Phys.* **2,** (2007).

8. Daniel, M.-C. & Astruc, D. Gold Nanoparticles: Assembly, Supramolecular Chemistry, Quantum-Size-Related Properties, and Applications toward Biology, Catalysis, and Nanotechnology. doi:10.1021/cr030698+

9. Faraday, M. The Bakerian Lecture: Experimental Relations of Gold (and Other Metals) to Light. *Philos. Trans. R. Soc. London* **147,** 145–181 (1857).

10. Logunov, S. L., Ahmadi, T. S., El-Sayed, M. A., Khoury, J. T. & Whetten, R. L. Electron Dynamics of Passivated Gold Nanocrystals Probed by Subpicosecond Transient Absorption Spectroscopy.

11. Prakash, J., Pivin, J. C. & Swart, H. C. Noble metal nanoparticles embedding into polymeric materials: From fundamentals to applications. *Adv. Colloid Interface Sci.* **226,** 187–202 (2015).

12. Rehbock, C. *et al.* Current state of laser synthesis of metal and alloy nanoparticles as ligand-free reference materials for nano-toxicological assays. *Beilstein J. Nanotechnol.* **5,** 1523–1541 (2014).

13. Hodkiewicz, J. & Scientific, T. F. Characterizing Carbon Materials with Raman Spectroscopy. *Prog. Mater. Sci.* **50,** 929–961 (2005).

14. Sakka, T., Oguchi, H. & Ogata, Y. H. Emission spectroscopy of ablation plumes in liquid for analytical purposes. *J. Phys. Conf. Ser.* **59,** 559–562 (2007).

15. Mohammadi, H. & Patten, J. A. Laser Augmented Diamond Drilling: A New Technique to Drill Hard and Brittle Materials. *Procedia Manuf.* **5,** 1337–1347 (2016).

16. Whittaker, A. G. Carbon : A New View of Its High-Temperature Behavior Published by : American Association for the Advancement of Science Stable URL : http://www.jstor.org/stable/1746626. **200,** 763–764 (1978).

17. Pan, B. *et al.* Carbyne with finite length: The one-dimensional sp carbon. *Sci. Adv.* **1,** 1–10 (2015).

18. Bawa, R. What's in a Name? Defining " Nano " in the Context of Drug Delivery 1. 978–981

19. Hirsch, A. The era of carbon allotropes. *Nat. Mater.* **9,** 868 (2010).

20. Sarkar, S., Bekyarova, E. & Haddon, R. C. Covalent chemistry in graphene electronics. *Mater. Today* **15,** 276–285 (2012).

21. Geim, A. K. & Macdonald, A. H. Graphene: Exploring carbon flatland. *Phys. Today* **60,** (2007).

22. Lee, J.-H., Loya, P. E., Lou, J. & Thomas, E. L. Dynamic mechanical behavior of multilayer graphene via supersonic projectile penetration. *Science (80-.).* **346,** 1092–1096 (2014).

23. Schütt, F. *et al.* Hierarchical self-entangled carbon nanotube tube networks. *Nat. Commun.* **8,** 1215 (2017).

24. Liu, M., Artyukhov, V. I., Lee, H., Xu, F. & Yakobson, B. I. Carbyne from First Principles: Chain of a Nanorod or a Nanorope. **7,** 10075–10082 (2013).

25. Liu, M., Artyukhov, V. I., Lee, H., Xu, F. & Yakobson, B. I. Carbyne from First Principles: Chain of a Nanorod or a Nanorope. *ACS Nano* **7,** 10075–10082 (2013).

26. Tykwinski, R. R. Carbyne: The Molecular Approach. *Chem. Rec.* **15,** 1060–1074 (2015).

27. Chalifoux, W. a & Tykwinski, R. R. Synthesis of polyynes to model the sp-carbon allotrope carbyne. *Nat. Chem.* **2,** 967–971 (2010).

28. Shi, L. *et al.* Confined linear carbon chains as a route to bulk carbyne. *Nat. Mater.* **15,** 634–639 (2016).

29. Tarakeshwar, P., Buseck, P. R. & Kroto, H. W. Pseudocarbynes: Charge-Stabilized Carbon Chains. *J. Phys. Chem. Lett.* **7,** 1675–1681 (2016).

30. Ganz, E., Ganz, A. B., Yang, L.-M. & Dornfeld, M. Carbon nanotube-carbyne composite: A nanoreactor in a quasi-1D liquid state. *Comput. Mater. Sci.* **149,** 409–415 (2018).

31. Barcikowski,S. Amendola, V. Marzun, G. Rehbock, C. Reichenberger, S. Zhang, D. Goekce, B. Handbook of Laser Synthesis of Colloids. 154 (2016). doi:http://dx.doi.org/10.17185/duepublico/41087

32. Zeng, H. *et al.* Nanomaterials via laser ablation/irradiation in liquid: A review. *Adv. Funct. Mater.* **22,** 1333–1353 (2012).

33. Spectra, P. Quanta-Ray PRO-Series. (2002).

34. Hollas, M. J. *Modern Spectroscopy*. (John Wiley & Sons, Inc., 1987).

35. George, F. & Smith. Maiman's Work. *IEEE J. Quantum Electron.* **20,** (1984).

36. Yan, Z. & Chrisey, D. B. Pulsed laser ablation in liquid for micro-/nanostructure generation. *J. Photochem. Photobiol. C Photochem. Rev.* **13,** 204–223 (2012).

37. Johnson, P. B. & Christy, R. W. Optical Constants of the Noble Metals. *Phys. Rev. B* **6,** 4370–4379 (1972).

38. Amendola, V. & Meneghetti, M. What controls the composition and the structure of nanomaterials generated by laser ablation in liquid solution? *Phys. Chem. Chem. Phys.* **15,** 3027–3046 (2013).

39. Dell'Aglio, M., Gaudiuso, R., De Pascale, O. & De Giacomo, A. Mechanisms and processes of pulsed laser ablation in liquids during nanoparticle production. *Appl. Surf. Sci.* **348,** 4–9 (2015).

40. De Giacomo, A. *et al.* Plasma processes and emission spectra in laser induced plasmas: A point of view ☆. *Spectrochim. Acta Part B At. Spectrosc.* **100,** 180–188 (2014).

41. Mościcki, T., Hoffman, J. & Szymański, Z. Modelling of plasma formation during nanosecond laser ablation. *Arch. Mech* **63,** 99–116 (2011).

42. MatterControl Manual contributors. MatterControl Manual. *MatterControl Manual* (2016). doi:2855

43. Rheims, J., Köser, J. & Wriedt, T. Refractive-index measurements in the near-IR using an Abbe refractometer. *Meas. Sci. Technol.* **8,** 601–605 (1997).

44. Scientific, C. Reversed Phase Chromatography. Available at: http://www.chromacademy.com/lms/sco5/Theory_Of_HPLC_Reverse_Phase_Chromatography.pdf. (Accessed: 28th March 2018)

45. RENISHAW. Raman Spectroscopy Explained. *RENISHAW -Apply Innov.* 1–44 (2017).

46. Kumar, S. Spectroscopy of Organic Compounds. *Dept. Chem.* **66,** 1–36 (2006).

47. Chamberlin, D. & Trutna, R. Physics of Particle Size Spectrophotometry.

48. Kolwas, K. & Derkachova, A. Damping rates of surface plasmons for particles of size from nano-to micrometers; reduction of the nonradiative decay. (2012).

49. Battie, Y., Resano-Garcia, A., Chaoui, N. & En Naciri, A. Optical properties of plasmonic nanoparticles distributed in size determined from a modified Maxwell-Garnett-Mie theory. *Phys. Status Solidi Curr. Top. Solid State Phys.*

12, 142–146 (2015).
50. Maetzler, C. Mie Result Gold. (2002).

51. Technospex. Introduction to Raman spectroscopy. Available at: www.technospex.com. (Accessed: 11th March 2018)

52. Moskovits, M. Persistent misconceptions regarding SERS. *Phys. Chem. Chem. Phys.* **15,** 5301 (2013).

53. Chu, Y., Banaee, M. G. & Crozier, K. B. Double-Resonance Plasmon Substrates for Surface-Enhanced Raman Scattering with Enhancement at Excitation and Stokes Frequencies. doi:10.1021/nn901826q

54. Kiefer, W., Mazzolini, A. P. & Stoddart, P. R. Recent Advances in linear and nonlinear Raman spectroscopy I. *J. Raman Spectrosc.* **38,** 1538–1553 (2007).

55. Axente, E. *et al.* Size distribution of Au NPs generated by laser ablation of a gold target in liquid with time-delayed femtosecond pulses. (2010).

56. Getting Started with Profit A Tool for Visualizing High-Resolution Spectra.

57. Zhou, P. Choosing the Most Suitable Laser Wavelength For Your Raman Application.

58. Hinz, A., Schulz, A. & Villinger, A. On the Behaviour of Biradicaloid [P(μ-NTer)]2 Towards Lewis Acids and Bases. *Chem. Commun.* **0,** 1–3 (2013).

59. Saito, R., Hofmann, M., Dresselhaus, G., Jorio, A. & Dresselhaus, M. S. Advances in Physics Raman spectroscopy of graphene and carbon nanotubes Raman spectroscopy of graphene and carbon nanotubes. *Adv. Phys.* **603,** 413–550 (2011).

60. Ferrari, A. C. Raman spectroscopy of graphene and graphite: Disorder, electron–phonon coupling, doping and nonadiabatic effects. *Solid State Commun.* **143,** 47–57 (2007).

61. Wesolowski, M. J. *et al.* Polyyne synthesis and amorphous carbon nano-particle formation by femtosecond irradiation of benzene. *Carbon N. Y.* **49,** 625–630 (2011).

62. Thongpool, V., Asanithi, P. & Limsuwan, P. Synthesis of carbon particles using laser ablation in ethanol. *Procedia Eng.* **32,** 1054–1060 (2012).

63. Casari, C. S. *et al.* Low-frequency modes in the Raman spectrum of sp-sp 2 nanostructured carbon.

64. Chernick, E. T. & Tykwinski, R. R. Carbon-rich nanostructures: The conversion of acetylenes into materials. *J. Phys. Org. Chem.* **26,** 742–749 (2013).

65. Welcome to the ImageJ Information and Documentation Portal 2/2. (2018).

APPENDIX A
DIFFRACTION SPACINGS FOR MATERIALS OF INTTEREST

Table A1: d-spacing's for nanosized gold spheres

2-Theta	Intensity	d-spacing	H	K	L	Multiplicity
38.28	100	2.351	1	1	1	8
44.5	47.92	2.036	2	0	0	6
64.75	28.36	1.4397	2	2	0	12
77.79	31.29	1.2278	3	1	1	24
81.97	8.94	1.1755	2	2	2	8

Table A2: Lattice spacings of known carbon materials

C- Materials	Composition	Spacing (Å)		
Carpathite	$C_{24}H_{12}$	10.035	4.695	16.014
Chaoite	C	8.948		14.078
Diamond	C	3.5595		
Dinite	$C_{20}H_{36}$			
Evenkite	$C_{21}H_{44}$	7.47	4.98	65.85
Fichtelite	$C_{19}H_{34}$	10.7	7.45	10.82
Flagstaffite	$C_{10}H_{22}O_3$	18.5	22.6	11
Graphene	C	1.42		
Graphite-2H	C	2.463		6.714
Graphite-3R	C	2.456		10.044
Hoelite	$C_{14}H_8O_2$			
Idrialite	$C_{22}H_{14}$	8.07	6.42	27.75
Kratochvílite	$C_{13}H_{10}$	8.47	5.7	18.87
Lonsdaleite	C	2.51		4.12
Naphthalene	$C_{10}H_8$			
Phylloretine	$C_{18}H_{18}$	6.26	8.52	23.45
Ravatite	$C_{14}H_{10}$	8.39	6.18	9.55
Simonellite	$C_{19}H_{24}$	9.231	9.134	36.01
Wampenite	$C_{18}H_{16}$	6.733	8.689	23.709